Simulating the one-dimensional structure of Titan's upper atmosphere: 2. Alternative scenarios for methane escape

Jared M. Bell,[1] Stephen W. Bougher,[2] J. Hunter Waite Jr.,[1] Aaron J. Ridley,[2] Brian A. Magee,[1] Kathleen E. Mandt,[3] Joseph Westlake,[3] Anna D. DeJong,[1] Virginie De La Haye,[1] Akiva Bar-Nun,[4] Ronen Jacovi,[5] Gabor Toth,[2] David Gell,[1] and Gregory Fletcher[1]

Received 28 April 2010; revised 8 September 2010; accepted 21 October 2010; published 30 December 2010.

[1] In Bell et al. (2010) (paper 1), we provide a series of benchmark simulations that validate a newly developed Titan Global Ionosphere-Thermosphere Model (T-GITM) and calibrate its estimates of topside escape rates with recent work by Cui et al. (2008), Strobel (2009), and Yelle et al. (2008). Presently, large uncertainties exist in our knowledge of the density and thermal structure of Titan's upper atmosphere between the altitudes of 500 km and 1000 km. In this manuscript, we explore a spectrum of possible model configurations of Titan's upper atmosphere that are consistent with observations made by the Cassini Ion-Neutral Mass Spectrometer (INMS), Composite Infrared Spectrometer, Cassini Plasma Spectrometer, Magnetospheric Imaging Instrument, and by the Huygens Gas Chromatograph Mass Spectrometer and Atmospheric Science Instrument. In particular, we explore the ramifications of multiplying the INMS densities of Magee et al. (2009) by a factor of 3.0, which significantly alters the overall density, thermal, and dynamical structures simulated by T-GITM between 500 km and 1500 km. Our results indicate that an entire range of topside CH_4 escape fluxes can equivalently reproduce the INMS measurements, ranging from $\sim 10^8 - 1.86 \times 10^{13}$ molecules m^{-2} s^{-1} (referred to the surface). The lowest topside methane escape rates are achieved by scaling the INMS densities by a factor of 3.0 and either (1) increasing the methane homopause altitude to ~1000 km or (2) including a physicochemical loss referred to as aerosol trapping. Additionally, when scaling the INMS densities by a factor of 3.0, we find that only Jeans escape velocities are required to reproduce the H_2 measurements of INMS.

Citation: Bell, J. M., et al. (2010), Simulating the one-dimensional structure of Titan's upper atmosphere: 2. Alternative scenarios for methane escape, *J. Geophys. Res.*, *115*, E12018, doi:10.1029/2010JE003638.

1. Introduction and Scientific Motivation

1.1. Methane Escape From Titan

[2] In an effort to understand the measurements made by the Cassini Ion-Neutral Mass Spectrometer (INMS) instrument, a series of papers has emerged that address the topside escape of H_2 and CH_4, sparking a debate within the Titan community. Some studies have suggested that large escape fluxes of both H_2 and CH_4 are required in order to explain the densities and mixing ratios measured by INMS [cf. *Cui et al.*, 2008; *Müller-Wodarg et al.*, 2008; *Strobel*, 2008, 2009; *Yelle et al.*, 2006, 2008]. While the calculated escape fluxes of H_2 are consistent with pre-Cassini estimates, the methane escape fluxes suggested by these works are far greater than pre-Cassini estimates [*Johnson et al.*, 2009].

[3] These authors collectively infer high outflows of CH_4 (but no outflow of N_2), which *Strobel* [2008] describes as slow, dense hydrodynamic escape of methane. The predicted escape fluxes range from 2.04×10^{13} CH_4 m^{-2} s^{-1} [*Strobel*, 2009] up to 3.00×10^{13} CH_4 m^{-2} s^{-1} [*Yelle et al.*, 2008], where all fluxes are referenced to the surface of Titan. This translates into a global methane loss rate of 2.7–4.0 $\times$ 10^{28} amu s^{-1}, or roughly 44–66 kg s^{-1} of methane flowing outward from Titan and into Saturn's magnetosphere. The

[1]Division of Space Science and Engineering, Southwest Research Institute, San Antonio, Texas, USA.
[2]Department of Atmospheric, Oceanic, and Space Sciences, University of Michigan, Ann Arbor, Michigan, USA.
[3]Department of Physics and Astronomy, University of Texas at San Antonio, San Antonio, Texas, USA.
[4]Department of Geophysics and Planetary Sciences, Tel Aviv University, Tel Aviv, Israel.
[5]Ice Spectroscopy Laboratory, Jet Propulsion Laboratory, California Institute of Technology, Pasadena, California, USA.

0148-0227/10/2010JE003638

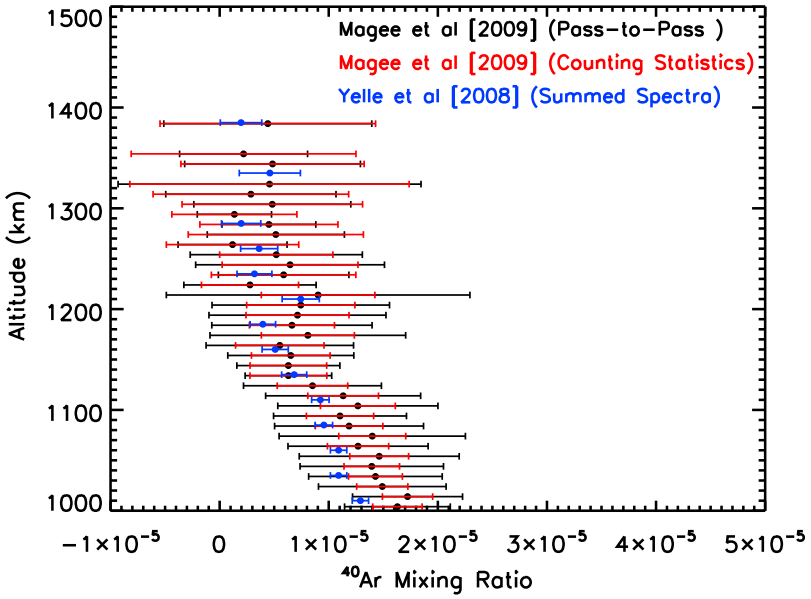

Figure 1. A comparison between the ^{40}Ar mixing ratios derived using the methods of *Magee et al.* [2009] and *Yelle et al.* [2008]. In black, we show the average INMS values from *Magee et al.* [2009]. The black horizontal lines represent the pass-to-pass variability in these values. The red horizontal lines represent the counting statistical uncertainties in the ^{40}Ar mixing ratios using the methods of *Magee et al.* [2009]. The blue circles and lines are those reported by *Yelle et al.* [2008], who employ a summed spectra approach.

calculated methane outflow rates are equivalent to between 20 and 30% of the total mass output of H_2O from the Enceladus plumes, which is currently estimated to be ~200 kg s^{-1} [*Porco et al.*, 2006; *Hansen et al.*, 2006]. Thus, these calculated CH_4 outflow rates represent a substantial source of neutral material to the Saturnian magnetosphere and should produce an observable methane group ion signature in the vicinity of Titan [*Johnson et al.*, 2009].

[4] However, measurements in the magnetosphere near Titan have not revealed methane group ions consistent with the outflow rates predicted by the hydrodynamic escape hypothesis [*Sittler et al.*, 2008]. The plasma measurements near Titan's orbit made by the Cassini Plasma Spectrometer (CAPS) Ion Mass Spectrometer (IMS) indicate that carbon ion densities are significantly less than those of either nitrogen or oxygen ion densities [*Crary et al.*, 2009, 2010]. Furthermore, recent observations by the Magnetospheric Imaging Instrument (MIMI) Charge Energy Mass Spectrometer (CHEMS) detects carbon ions at ~1.3% relative to the oxygen ions near Titan's orbit [*Smith et al.*, 2009]. While both the MIMI and CAPS magnetospheric measurements are indirect constraints upon the neutral mass outflow from Titan, they together suggest an upper limit of ~1 × 10^{26} amu s^{-1}(~1.1 × 10^{11} CH_4 m^{-2} s^{-1}).

[5] In addition to the lack of measured methane group ions in Saturn's magnetosphere near Titan's orbit, exospheric modeling by *Tucker and Johnson* [2009], using a Direct Simulation Monte Carlo (DSMC) investigation, indicates that there is not sufficient energy to accelerate CH_4 to the high escape speeds required by hydrodynamic escape. Even after increasing the exobase temperature to 600 K and after adding an additional upward heat flux of 4.8 × 10^8 eV cm^{-2} s^{-1}, they are unable to reproduce escape fluxes consistent with the hydrodynamic hypothesis [see also *Johnson et al.*, 2009]. This leads *Tucker and Johnson* [2009] to conclude that thermal escape is not sufficient and, if escape fluxes consistent with hydrodynamic escape are occurring, then they are most likely driven by either nonthermal mechanisms or the global circulation of the planet.

[6] Thus, an inconsistency exists between theoretical explanations of INMS data and the measurements made in the near-Titan magnetosphere by CAPS IMS and MIMI CHEMS. This investigation seeks to reconcile this inconsistency by (1) reproducing the INMS measurements of N_2, CH_4, and H_2 with high accuracy and (2) doing so without requiring hydrodynamic-like CH_4 escape fluxes. In order to accomplish this, we must investigate the current uncertainties in our understanding of Titan's upper atmosphere. Moreover, we assess (in models 6 and 9) the role of a process known as aerosol trapping, which functions as a physicochemical sink for methane and nitriles in Titan's atmosphere (see section 2.1). Throughout our investigation, we evaluate the simulations of Titan's upper atmosphere according to (1) how well they match the INMS data reported by *Magee et al.* [2009] and (2) whether or not the predicted CH_4 topside escape rates are consistent with upper limits imposed by CAPS and MIMI.

1.2. INMS Data

[7] As discussed by *Bell et al.* [2010], hereafter referred to as paper 1, currently two independent methods exist to analyze the Cassini INMS raw data: that of *Cui et al.* [2009] and that of *Magee et al.* [2009]. The details of both methods and their differences are beyond the scope of the current work, and we encourage the reader to seek more information from the thorough comparison made by *Magee et al.* [2009]. While both analyses agree in their major species' neutral densities, they differ in their minor species' abundances.

These differences can have significant scientific implications. In particular, the derived ^{40}Ar volume mixing ratios differ substantially between the two methods, resulting in different implied homopause altitudes, as shown in Figure 1.

[8] Figure 1 illustrates the ^{40}Ar mixing ratios derived using the methods of *Magee et al.* [2009] and those reported by *Yelle et al.* [2008]. We denote the average ^{40}Ar mixing ratios of *Magee et al.* [2009] as the black circles and the pass-to-pass variability (uncertainty) in these values by the horizontal black lines. In addition to this, there is also an uncertainty due to counting statistics, which is quantified by the horizontal red lines. Please note that, above 1150 km, the uncertainties in the Argon mixing ratios grow so large that they encompass negative values, meaning that INMS can only provide upper limits to the ^{40}Ar mixing ratios. By contrast, the Argon mixing ratios of *Yelle et al.* [2008] are depicted by the blue circles and the associated precision values by the horizontal blue lines, which show a reduced overall uncertainty in the values relative to those of *Magee et al.* [2009].

[9] This discrepancy is straightforward to explain. *Yelle et al.* [2008] note that the extracted ^{40}Ar densities (and mixing ratios) possess a low signal-to-noise ratio (SNR) and, therefore, high uncertainties for any given flyby. In order to improve this SNR, the authors average together several flyby spectra at a given altitude, increasing the counts at M/Z = 40 and reducing the overall uncertainty in the extracted ^{40}Ar densities and mixing ratios. The results of this process are shown as the blue data points and horizontal bars in Figure 1. While these extracted mixing ratios possess lower overall uncertainties, the process of coadding several flyby spectra together at a given altitude precludes the possibility of propagating the individual flyby counting statistical uncertainties through to the final result. In effect, this method of coadding spectra assumes that the distribution of ^{40}Ar sampled by INMS is spatially and temporally uniform (i.e., that INMS is sampling the same ^{40}Ar distribution at different latitudes, longitudes, and at different times over the course of the Titan flybys).

[10] While coadding spectra to get better precision from the extracted mixing ratios represents one approach, we employ another method that can be summarized by the following steps: (1) take the INMS measurements of ^{40}Ar and its associated counting statistical uncertainties for each flyby between TA and T40, (2) separate the data into 10 km bins in the vertical, (3) average the data within each vertical bin, (4) propagate the counting statistical uncertainties from all data points within each bin to produce a combined counting statistical error, and (5) quantify the amount of pass-to-pass variation within each bin (i.e., the standard deviation of the binned data).

[11] This new method does not assume that the ^{40}Ar distribution is uniform in time and space, and, in fact, quantifies the flyby-by-flyby variations present in the INMS retrievals for the Argon mixing ratios and densities. The results from this second method are shown in Figure 1, where we separately quantify the propagated counting statistical uncertainties (red horizontal lines) and the uncertainties due to pass-to-pass variability (the black horizontal lines).

[12] These pass-to-pass variations are composed of several sources: (1) time-dependent geophysical variations in Titan's atmosphere, (2) latitudinal and local time variations among the different trajectories, and (3) systematic errors in measurements independent of a signal-to-noise uncertainty. As shown in Figure 1, these additional sources of uncertainty are significant and, as we show later, they have important scientific implications. We note also that this binning method, through the propagation of errors, increases the overall uncertainties by averaging the ^{40}Ar data products. In contrast, the method of *Yelle et al.* [2008] reduces the overall uncertainties in their derived ^{40}Ar data products by coadding spectra to increase their signal-to-noise ratio. Despite the differences between the two methods, we maintain that they are both valid approaches, and we view Figure 1 as an illustration of the difficulties inherent in deriving meaningful minor species abundances from the raw data. We encourage readers to seek out both *Cui et al.* [2009] and *Magee et al.* [2009] for a more exhaustive treatment of this broader problem.

[13] Although two robust methods exist for analyzing the Cassini INMS raw data, they produce data products that are currently inconsistent with other instruments. The Titan Atmospheric Working Group (TAMWG) has suggested that the INMS-derived densities are likely too low by roughly a factor of 3. Measurements from the Cassini Attitude and Articulation Control System (AACS) and the Navigation (NAV) provided evidence for this claim [*Lee and Hanover*, 2005; *Sarani and Lee*, 2009]. *Strobel* [2009] points out that the Huygens Atmospheric Science Instrument (HASI) neutral densities are also a factor of 2.5 greater than those measured by INMS in overlapping altitudes, further bolstering the possibility that INMS may be systematically too low by a factor of 2.5–3.0. We explore the ramifications of increasing the INMS densities by a multiplicative factor of 3.0, and we show that it has significant scientific implications for the interpretation of the mass loss processes in Titan's upper atmosphere.

2. Titan Global Ionosphere-Thermosphere Modeling Framework

[14] The numerical details of the Titan Global Ionosphere-Thermosphere Model (T-GITM) are presented in paper 1 and will not be repeated here. This model is based upon an existing Earth Global Ionosphere-Thermosphere Model (GITM), developed at the University of Michigan [*Ridley et al.*, 2006]. This newly developed model is nonhydrostatic, meaning that it does not enforce the hydrostatic equilibrium condition, and it employs spherical polar coordinates, using altitude as the vertical coordinate.

[15] T-GITM is composed of 15 neutral species, 5 ionic species, and an electron population equal to the total ion density. The neutral constituents consist of 10 primary species that each possess their own continuity and momentum equations (N_2, CH_4, ^{40}Ar, HCN, H_2, $^{13}CH_4$, ^{15}N-^{14}N, $N(^4S)$, H, and C_2H_4). The 5 remaining neutral species ($^3CH_2$, $^1CH_2$, CH_3, CH, and H_2CN) are not advected, responding only to chemical sources and sinks. The 5 ionic species in T-GITM (N_2^+, N^+, $HCNH^+$, CH_3^+, and $C_2H_5^+$) possess individual continuity and momentum equations as described by *Ridley et al.* [2006]. Finally, the electrons provide neutrality to the ionosphere and there is currently no

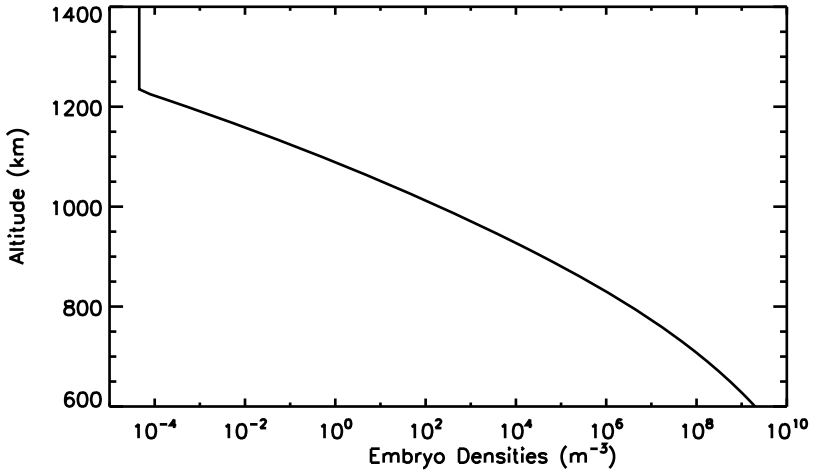

Figure 2. Vertical profile of the aerosol embryos that are responsible for trapping the background gas. These represent the Class A species from *Bar-Nun et al.* [2008].

separate calculation for electron temperature, velocities, or densities enabled.

2.1. Including Aerosol Trapping and Heterogeneous Processes in T-GITM

[16] In paper 1, we detail the chemical reactions currently implemented in Titan GITM (see Figure 1 of paper 1). The chemical scheme ends at the formation of C_2H_4; however, the complex chemistry at Titan continues well beyond this, forming large hydrocarbons that are measured at high altitudes as neutrals by INMS [*Waite et al.*, 2007] and as heavy negative ions by the CAPS Electron Spectrometer (ELS) [*Coates et al.*, 2007]. The formation of these larger hydrocarbons is the focus of an extensive literature in photochemical modeling at Titan [cf. *De La Haye et al.*, 2008b; *Krasnopolsky*, 2009; *Lavvas et al.*, 2008a, 2008b; *Sekine et al.*, 2008a, 2008b; *Waite et al.*, 2007; *Wilson and Atreya*, 2004].

[17] *Bar-Nun et al.* [2008] refers to these high-altitude, large hydrocarbons as nascent "aerosol embryos," which grow through the addition of more polymer chains and through the coalescence of small particles. Eventually, these aerosol embryos form the haze layers that are prominent in Titan's atmosphere. The high-altitude aerosol embryos, due to their large mass relative to the surrounding atmospheric gases descend through the atmosphere, coalescing and growing as they drop in altitude. Over the last decade, a detailed microphysical energy-dependent description of aerosol embryo production, agglomeration, and evolution has been developed by *Dimitrov and Bar-Nun* [1999, 2002, 2003].

[18] Results from these detailed modeling studies demonstrate that the vertical distribution of aerosols deep in the atmosphere (i.e., below 500 km) are highly sensitive to the aerosol embryo densities in the thermosphere (above 700 km). Recently, this model has been validated by directly comparing its results against the measurements by the Descent Imager/Spectral Radiometer (DISR) in the work of *Bar-Nun et al.* [2008]. This comparison suggested that the aerosol densities of *Bar-Nun et al.* [2008] high in the thermosphere represent a reasonable approximation to the equilibrium state of the aerosol embryos.

[19] Given this validation, we employ the model results from *Bar-Nun et al.* [2008] as a static representation of the aerosol embryo equilibrium vertical distribution in T-GITM. Figure 2 depicts the adopted aerosol embryo densities as a function of altitude, and this is an interpolated curve matching the "Class A" particles of *Bar-Nun et al.* [2008]. Please note that the embryo densities drop below an interpolation threshold value, producing a nonphysical distribution above 1200 km. However, adjustments to the aerosol densities in this altitude regime have very little impact on the column-integrated trapping rates.

[20] Constraining the equilibrium aerosol embryo densities high in the thermosphere is only a component of the aerosol trapping mechanism. In addition to this, the heterogeneous interaction between the aerosol and the atmospheric gases can be characterized by a trapping efficiency. These aerosol trapping efficiencies, which are shown in Table 1, are completely analogous to the trapping of gaseous material in amorphous ices [*Bar-Nun et al.*, 2007]. In the case of aerosol embryos, the open lattice structure of the nascent aerosols allows them to trap atmospheric gases. In particular, *Jacovi and Bar-Nun* [2008] demonstrate experimentally that these aerosol embryos can trap noble gases, which are nonreactive and weakly polarizable. Moreover, they illustrate that this trapping by aerosols can explain the low abundance of key noble gases in Titan's upper atmosphere, namely: Ar, Kr, and Xe. Given this result, aerosols cages, in complete analogy with amorphous ice, can also trap more reactive and polar molecules (such as CH_4 and HCN) more easily than the very weakly polarizable noble gases.

Table 1. Aerosol Trapping Efficiencies Used in T-GITM Taken From *Jacovi and Bar-Nun* [2008], *Bar-Nun et al.* [2007], and *Bar-Nun and Kleinfeld* [1989]

	CH_4	N_2	HCN	^{40}Ar	H_2
Trapping efficiency	1.0×10^{-2}	1.43×10^{-6}	1.0×10^{-2}	3.5×10^{-4}	0

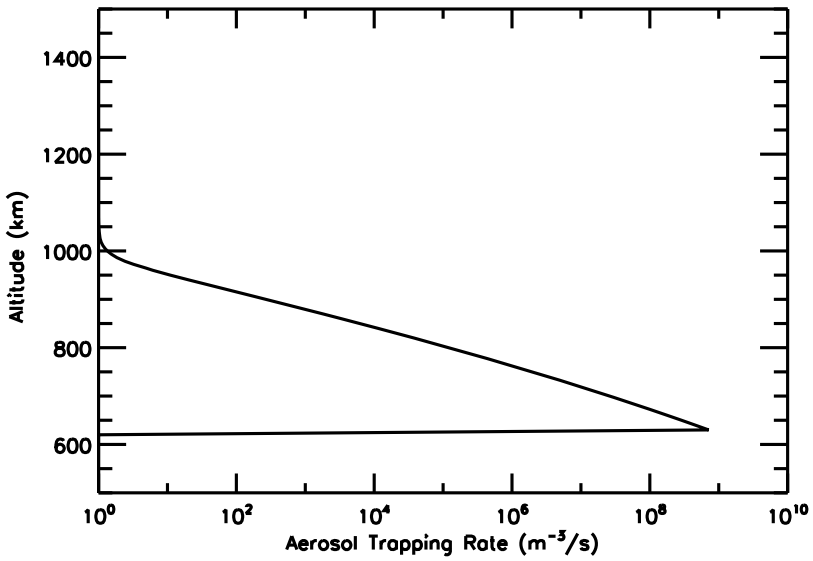

Figure 3. Simulated aerosol trapping rates for model 6 (see section 3.1), depicting the typical variation in aerosol trapping rates with altitude in T-GITM.

[21] In particular, the polar C-H bonds in CH_4 interact more strongly with the hydrocarbon aerosols. Thus, just as in the amorphous ice case, one can expect that CH_4's trapping efficiency in aerosol cages is roughly 100 times greater [see *Notesco and Bar-Nun*, 1997; *Bar-Nun et al.*, 2007] than the equivalent Argon trapping efficiencies measured by *Jacovi and Bar-Nun* [2008]. This means that methane is most likely trapped with an efficiency between 3.5% and 4%. However, in order to make the present study as conservative as possible, we employ a significantly reduced trapping efficiency of only 1%. Similarly, HCN, due to its polarizability, is more easily trapped in the aerosol embryo cages (consistent with the measured trapping by amorphous ice). Again, as shown in Table 1, we use a very conservative 1% trapping efficiency for HCN. We note that similar aerosol interaction efficiencies are used in the study by *Liang et al.* [2007], suggesting that we have chosen reasonably conservative, yet experimentally validated aerosol trapping efficiencies.

[22] In order to parameterize the microphysics of aerosol trapping efficiently in T-GITM, we combine the vertical profile of aerosol embryo densities from *Bar-Nun et al.* [2008] and Figure 2 with experimentally determined trapping efficiencies [*Jacovi and Bar-Nun*, 2008] into a physicochemical mechanism for methane loss in Titan's upper atmosphere that we term aerosol trapping. In the model, aerosol trapping is included as a secondary process, separate from the initial photochemical loss of methane. Thus, we implement a two-stage loss mechanism for CH_4 (and other gases): (1) first, methane is photodissociated and the subsequent complex chemistry results in the eventual formation of the aerosol embryos in Figure 2 and then (2) these aerosol cages, once formed, begin to trap the background gases (especially CH_4 and HCN) in their lattice structures analogous to amorphous ice [*Jacovi and Bar-Nun*, 2008]. In order to calculate the aerosol trapping rates, the collision frequency between these descending aerosol particles and the background gases is approximated as hard sphere collisions. The aerosol trapping rates are then calculated as follows:

$$L_{aero,s} = N_{aero}^{carbon} n_{aero} \nu_{aero,s} \epsilon_s, \quad (1)$$

where $L_{aero,s}$ represents the aerosol trapping rate (in m^{-3} s^{-1}) of species "s," N_{aero}^{carbon} is the mean number of Carbon atoms in the aerosol [see *Bar-Nun et al.*, 2008], n_{aero} is the aerosol density (m^{-3}), $\nu_{aero,s}$ represents the hard sphere collisional frequency (in Hz) between the aerosol embryo and species "s," and ϵ_s represents the aerosol trapping efficiency for species "s" (compare Table 1).

[23] A sample aerosol trapping loss function from model 6 (see section 3.1) is shown in Figure 3. The sharp cutoff at ~625 km is imposed to limit the aerosol trapping below 700 km. The aerosols cease trapping between 500 km and 700 km, because their open lattice structure begins to transition to a more closed structure. This transition is referred to as hardening by *Bar-Nun et al.* [2008]. For the purposes of our work here, this hardening of the aerosols means that they no longer trap atmospheric gases efficiently in T-GITM, and we must account for this by imposing a cutoff in the trapping rates. We note that the sharpness of this aerosol trapping cutoff is artificial in Figure 3, but the shape of this curve does not materially affect the simulations. Instead, T-GITM responds only to the column-integrated aerosol trapping rates. Lastly, we note that this transition region is diffuse, allowing us to adjust these cutoff altitudes in models 6 and 9 (see sections 3.1 and 3.2),so that we may increase or decrease the total column-integrated aerosol trapping rates.

[24] Physicochemical (i.e., heterogeneous) interactions between atmospheric gases and aerosols is well established in Titan's upper atmosphere. *Lebonnois et al.* [2003] finds that heterogeneous chemistry, which is the chemical exchange between suspended aerosols and the gas phase atmosphere, represents an important component of H conversion into H_2. This was corroborated by the work of

Table 2. Global Parameter Settings Used in All Simulations

Parameter	Setting in T-GITM
$F_{10.7cm}$ radio flux	70.0×10^{-22} W m^{-2} Hz^{-1}
Subsolar latitude	13°S
Model latitude	45°N
Model longitude	0°N

Lavvas et al. [2008a, 2008b] and *Sekine et al.* [2008a, 2008b]. We include this heterogeneous conversion of H into H_2 as a chemical source, adopting the formulation of *Lebonnois et al.* [2003]. Thus, the physical-chemical losses due to aerosol trapping represent a natural extension and outgrowth of the already-established hydrogen heterogeneous chemistry. A process similar to aerosol trapping is outlined by *Liang et al.* [2007], where atmospheric gases are removed by aerosol adsorption. The novel aspect of the work presented here is that we quantify the amount of aerosol trapping (in terms of a column-integrated loss rate) that is necessary to reproduce the observations by the INMS instrument.

2.2. Boundary Conditions and Settings for T-GITM

[25] As with the numerics of T-GITM, the details of the boundary conditions used in the model have been discussed in paper 1, so the reader is referred to that paper. The global parameter settings, such as solar activity level, are summarized in Table 2 and they are held constant throughout the simulations of this investigation. In order to model realistic configurations of Titan's upper atmosphere, we use recent Cassini-Huygens measurements as inputs for the lower boundary conditions. Tables 3 and 4 provide an overview of how we constrain the model using Cassini mission measurements. As shown in Table 3, several investigations are used provide realistic lower boundary settings for T-GITM. These settings then play a major role in determining the converged temperature, density, and vertical wind structures. Similarly, Table 4 describes the Cassini-Huygens measurements to which we compare the T-GITM output fields.

[26] While Tables 3 and 4 provide a general overview of how we constrain the Titan-GITM, the details of the lower boundary settings are given in Table 5. These settings are specified in the ghost cells below 500 km, where we set the densities (or equivalently, the mixing ratios) and velocities for each species and their temperatures as follows: (1) N= N_0 and $\chi_s = \chi_{s,0}$, (2) T = T_0, and (3) $V_s = 0.0$.

[27] N is the total density (in m^{-3}), χ_s is the mixing ratio for the individual species, T is the temperature (in K), and V_s is the vertical (radial) velocity (in m s^{-1}). We assume that these lower boundary constraints remain constant over the course of the simulation. Similarly, at the top of the model (at 1500 km), we impose the following boundary conditions: (1) $\frac{1}{n_s}\frac{\partial n_s}{\partial r} = -\frac{1}{H_s}$, (2) $\frac{\partial T}{\partial r} = 0.0$, and (3) $\frac{\partial V_s}{\partial r} = 0.0$ or $V_s = V_{escape}$.

[28] Thus, at 1500 km, we impose diffusive equilibrium on the neutral densities, which may not be appropriate for escaping species such as H_2. We also assume that the temperature gradient is 0.0 at 1500 km. Finally, we may either adopt a zero vertical velocity gradient, or we can impose an escape velocity when it is needed. Table 6 outlines some of the key topside boundary conditions for the simulations of this study. In Table 6, we enumerate the escape fluxes of H_2 and CH_4 used in each simulation and whether or not the velocity upper boundary condition is set according to $V_s = V_{escape}$ or $\frac{dV_s}{dr} = 0$.

Table 3. Key Lower Boundary Inputs Into the T-GITM Model Provided by Cassini Mission Instruments[a]

Constraint for T-GITM	Where It Is Employed	Relevant Instrument(s)
Total neutral density	500 km	HASI and CIRS
Temperature	500 km	HASI and CIRS
CH_4 mixing ratio	500 km	GCMS and CIRS
H_2 mixing ratio	500 km	GCMS and CIRS
^{40}Ar mixing ratio	500 km	GCMS

[a]These settings drive the simulations in this investigation.

2.3. Constraining Turbulence Using ^{40}Ar

[29] As discussed in paper 1, the radiogenic isotope ^{40}Ar is measured in the upper atmosphere and remains chemically inert, meaning that it functions as an independent constraint on the eddy diffusion profile. Throughout this investigation, we rely upon two formulations for turbulent mixing in the upper atmosphere of Titan. The primary method involves a coefficient that varies with altitude according to *Atreya* [1986] and is given by

$$K(r) = K(0)\sqrt{\frac{N(0)}{N(r)}}, \quad K \le K_{\max}. \tag{2}$$

[30] In this equation, $K(0)$ and $N(0)$ represent the eddy diffusion coefficient and the total neutral density at the model's lower boundary, respectively, while $K(r)$ and $N(r)$ represent the same parameters at a specific radial distance, r. Finally, K_{max} is the maximum, asymptotic value for K(r) allowed in a given simulation. The parameters K(0) and K_{max} are given Table 5. As discussed by *Krasnopolsky* [2009], this turbulence formulation accounts for the eddy diffusion induced by upward propagating gravity waves and tides not explicitly resolved by the model. For the purposes of comparing with recent work, we also employ a second formulation for turbulence in a limited series of simulations (models 3, 3(NC), and 10), adapted from *Yelle et al.* [2008] and utilized in paper 1:

$$K(r) = \frac{K_0 K_\infty (p_0/p(r))^\gamma}{K_0 (p_0/p(r))^\gamma + K_\infty}, \tag{3}$$

where $K_0 = 3.0 \times 10^{-4}$ m^2 s^{-1}, $p_0 = 1.43$ dyne cm^{-2}, $K\infty$ =

Table 4. Key Outputs From T-GITM and the Cassini-Huygens Instrument(s) Against Which We Compare the Simulation Results

Output Field From T-GITM	Altitude Range	Relevant Comparison Measurement
Neutral densities	1000 km – 1400 km	INMS densities
Total density	500 km – 1000 km	HASI densities
Neutral mixing ratios	1000 km – 1400 km	INMS mixing ratios
Temperatures	500 km – 1000 km	HASI temperatures
Topside escape fluxes of CH_4	1500 km	CAPS/MIMI inferred escape rates

Table 5. Summary of Lower Boundary Settings in the T-GITM Simulations[a]

	Lower Boundary Settings at 500 km					Turbulence Settings		Aerosol Trapping
	Total Density (molecules m^{-3})	T (K)	CH_4 Mixing Ratio	H_2 Mixing Ratio	^{40}Ar Mixing Ratio	K_0 (m^2 s^{-1})	K_{max} (m^2 s^{-1})	Integrated Rate (molecules m^{-2} s^{-1})
Model 3	4.80×10^{19}	160	1.23×10^{-2}	3.2×10^{-3}	4.15×10^{-5}	932.0 (Y)	3200.0	N/A
Model 4	4.80×10^{19}	160	1.23×10^{-2}	3.2×10^{-3}	4.15×10^{-5}	350.0 (A)	30,000.0	N/A
Model 5	4.80×10^{19}	160	1.23×10^{-2}	3.2×10^{-3}	3.36×10^{-5}	500.0 (A)	300,000.0	N/A
Model 6	4.80×10^{19}	160	1.16×10^{-2}	3.2×10^{-3}	4.15×10^{-5}	350.0 (A)	30,000.0	3.2×10^{13}
Model 7	7.74×10^{19}	180	1.23×10^{-2}	3.35×10^{-3}	4.15×10^{-5}	175.0 (A)	30,000.0	N/A
Model 8	7.55×10^{19}	180	1.30×10^{-2}	3.50×10^{-3}	3.50×10^{-5}	235.0 (A)	N/A	N/A
Model 9	7.74×10^{19}	180	1.16×10^{-2}	3.35×10^{-3}	4.15×10^{-5}	175.0 (A)	30,000.0	0.697×10^{13}
Model 10	7.74×10^{19}	180	1.23×10^{-2}	3.35×10^{-3}	4.15×10^{-5}	289.9 (Y)	1412.4	N/A

[a]A and Y associated with the K_0 refer to the *Atreya* [1986] and *Yelle et al.* [2008] methods for calculating K(r), respectively. K_{max} is the maximum, asymptotic value of the K(r) permitted in that simulation (N/A in that column means that no maximum was enforced). The aerosol trapping rates are column-integrated trapping rates of methane, scaled relative to the surface (N/A in the last column means that aerosol trapping is not included).

3000.0 m^2 s^{-1}, and $\gamma = 0.90$. Both K(0) and $K_{max} = K\infty$ are given in Table 5.

3. Scientific Results

[31] This section presents a series of one-dimensional simulations that span a large parameter space. We seek configurations of Titan's upper atmosphere that are consistent with both the INMS measurements [*Magee et al.*, 2009] and the upper limits on the CH_4 escape rates imposed by CAPS and MIMI observations [*Crary et al.*, 2010; *Smith et al.*, 2009]. We proceed by systematically adjusting three global parameters: (1) the scaling of the INMS densities by 1.0 or 3.0 relative to those of *Magee et al.* [2009], (2) the altitude of the ^{40}Ar homopause (840 km, 940 km, or 990 km), and (3) the inclusion of aerosol trapping (included or not included). Only two simulations employ aerosol trapping: model 6 of section 3.1 and model 9 of section 3.2.

[32] In section 3.1, we present simulations compared against the INMS measurements of *Magee et al.* [2009] without any scaling factor. We sometimes refer to those as the unscaled INMS cases. In section 3.2, we present an analogous set of model calculations compared against the INMS densities scaled by a multiplicative factor of 3.0. We sometimes refer to these simulations as the scaled INMS cases. Finally, we also reintroduce two model simulations from paper 1, models 3 and 3(NC), which represent analogues to the recent work by *Cui et al.* [2008], *Strobel* [2009], and *Yelle et al.* [2008].

[33] Tables 5 and 6 provide the details of each simulation's lower and upper boundaries, respectively. Meanwhile, Table 7 provides a more general overview of the simulations in this section. Table 7 organizes the different models of sections 3.1 and 3.2 according to whether or not the simulation matches the unscaled INMS densities (Table 7, left) or the INMS densities scaled by a factor of 3.0 (Table 7, right). Moreover, we have organized the simulations in each column in order of increasing methane homopause altitudes.

[34] For each simulation listed in Table 7, we have provided the topside methane escape fluxes (relative to the surface) required to match the INMS data as well as the methane homopause altitude. We have also quantified the column-integrated aerosol trapping rates employed (if applicable), referenced to the surface. We have also included the relevant entries from both *Yelle et al.* [2008] and *Strobel* [2009] for comparison. Table 7 highlights the three major determining factors impacting the estimated CH_4 escape rates necessary to match INMS composition: (1) whether we are matching the scaled or the unscaled INMS densities of *Magee et al.* [2009], (2) the methane homopause altitudes, and (3) the column-integrated amount (if any) of aerosol trapping included.

[35] We compare the T-GITM simulated densities and mixing ratios to those of INMS in Table 8, using the same methodologies as in paper 1. This method involves creating

Table 6. Key T-GITM Boundary Settings at 1500 km[a]

	Topside Boundary Settings at 1500 km				
	Q_{Plasma} (eV cm^{-3} s^{-1})	Φ_{H_2} (molecules $m^{-2}s^{-1}$)	Φ_{CH_4} (molecules $m^{-2}s^{-1}$)	CH_4 Escape Flux Boundary Condition	CAPS and MIMI Inferred Escape Rates (CH_4 $m^{-2}s^{-1}$)
Model 3	0.0	1.06×10^{14}	1.86×10^{13}	Enforced	$1.0 - 2.0 \times 10^{11}$
Model 4	90.0	1.03×10^{14}	9.59×10^{12}	Enforced	$1.0 - 2.0 \times 10^{11}$
Model 5	45.0	1.01×10^{14}	4.17×10^{12}	Enforced	$1.0 - 2.0 \times 10^{11}$
Model 6	95.0	9.67×10^{13}	4.85×10^{12}	Enforced	$1.0 - 2.0 \times 10^{11}$
Model 7	115.0	1.08×10^{14}	3.24×10^{12}	Enforced	$1.0 - 2.0 \times 10^{11}$
Model 8	80.0	1.07×10^{14}	$< 1.0 \times 10^{08}$	Self-consistent	$1.0 - 2.0 \times 10^{11}$
Model 9	115.0	1.07×10^{14}	$< 1.0 \times 10^{08}$	Self-consistent	$1.0 - 2.0 \times 10^{11}$
Model 10	0.0	1.04×10^{14}	1.25×10^{13}	Enforced	$1.0 - 2.0 \times 10^{11}$

[a]The first column is the imposed heating function (denoted Q_{plasma}) at 1500 km. The topside escape fluxes, Φ_{CH_4}, and Φ_{H_2} are referred to the surface of Titan. The fourth column indicates the type of boundary condition used to match the INMS CH_4 densities, either Enforced, the topside escape rates of methane are enforced upon T-GITM as a boundary condition ($V_s = V_{escape}$), or self-consistent, the escape fluxes are simulated by T-GITM self-consistently (i.e., the model adopts the boundary condition of $\frac{\partial V_s}{dr} = 0.0$). Finally, the inferred escape rates from the combined CAPS and MIMI investigations are presented.

Table 7. A Summary of the Key Differences Between the Different Models and the Associated Topside Escape Rates of CH_4 Referenced to the Surface[a]

Unscaled INMS Data				Scaled INMS Data				
Model	Φ_{CH_4} (CH_4 m^{-2} s^{-1})	Homopause Altitude (km)	Aerosol Trapping (CH_4 $m^{-2}s^{-1}$)	Model	Φ_{CH_4} (CH_4 m^{-2} s^{-1})	Homopause Altitude (km)	Aerosol Trapping (CH_4 m^{-2} s^{-1})	^{40}Ar Data Set
Model 3 (NC)	2.64×10^{13}	840.0	N/A					Yelle
Model 3	1.86×10^{13}	840.0	N/A	Model 10	1.25×10^{13}	850.0	N/A	Yelle
Model 4	9.59×10^{12}	940.0	N/A	Model 7	3.24×10^{12}	950.0	N/A	Magee
Model 5	4.17×10^{12}	980.0	N/A	Model 8	$<1.0 \times 10^{08}$	990.0	N/A	Magee
Model 6	4.85×10^{12}	940.0	3.2×10^{13}	Model 9	$<1.0 \times 10^{08}$	950.0	0.697×10^{13}	Magee
Yelle et al. [2008]	$2.5 - 3.0 \times 10^{13}$	840.0	N/A					Yelle
Strobel [2009]	2.04×10^{13}	~840.0	N/A					Yelle

[a]Homopause altitudes are for methane. The aerosol trapping rates are column-integrated trapping rates referenced to the surface (N/A indicates that aerosol trapping is not used in that model configuration). The final column on the right hand side contains the ^{40}Ar data that constrains that model: Yelle for *Yelle et al.* [2008] and Magee for *Magee et al.* [2009].

average INMS profiles from the flyby trajectories between TA and T40. Furthermore, we interpolate this average data onto the 10 km vertical grid of T-GITM in order to provide a direct comparison with the simulated fields. Section 3 in paper 1 contains a more detailed discussion.

3.1. The 1-D T-GITM Compared With the Unscaled INMS Densities

[36] We now compare five simulations against the averaged INMS data of *Magee et al.* [2009]. The five model runs of this section are labeled models 3, 3(NC), 4, 5, and 6 in Figures 4–7 and in Tables 5–8. In Table 7 (left), we have provided a general overview of the model configurations in this section, separated by methane homopause altitude and whether or not they include aerosol trapping. Meanwhile, Tables 5 and 6 provide more detailed settings for each simulation. In models 3 and 3(NC), we utilize the ^{40}Ar mixing ratios and the eddy diffusion coefficient of *Yelle et al.* [2008], while also imposing an artificial maximum abundance on HCN of 1.9×10^{-4}. Model 3(NC) also ignores the chemical losses on CH_4, in analogy with assumptions made by *Yelle et al.* [2008]. These simulations are taken directly from paper 1, and we utilize them in this investigation as the proxies for previous work by *Yelle et al.* [2008] and *Strobel* [2009].

[37] Model 4, which we sometimes refer to simply as (Magee), possesses the full chemistry found in Figure 1 of paper 1, and is constrained to match the ^{40}Ar mixing ratios of *Magee et al.* [2009]. Model 4 requires external heating rates of 90.0 eV cm^{-3} s^{-1} in order to balance the HCN cooling. These settings make model 4 analogous to model 1 in paper 1, except model 4 possesses a new eddy diffusion profile and a higher homopause altitude. Next, model 5 (LB Argon) is identical to model 4, except now the ^{40}Ar mixing ratios at 500 km are reduced by 20%. This adjustment means that, when matching the Argon data of *Magee et al.* [2009], a higher homopause is allowed. Last, model 6 (Aerosols) is identical in setup to model 4, except now aerosol trapping is implemented as a loss process for the atmospheric species listed in Table 1. Both models 5 and 6 employ the same chemistry as model 4 and also require external heating rates imposed at 1500 km, the values of which are found in Table 6.

[38] The simulated major neutral densities of models 3, 4, 5, and 6 are shown in Figure 4a, for N_2, CH_4, and H_2. Figure 4b shows the associated mixing ratios of CH_4 and H_2. As seen in Table 8 and Figure 4, models 3, 4, 5, and 6 equivalently reproduce the averaged INMS neutral density and mixing ratio measurements, each possessing comparable percentage deviations in all of the relevant fields. Please note that we do not show model 3(NC) fields explicitly on Figures 4a and 4b, because they overlap with model 3 so closely that they are simply redundant information.

[39] Figure 5a contains the thermal structures for the simulations of this section and they are very similar to those discussed in paper 1. Figure 5b depicts the location of the nominal homopause for both CH_4 and H_2, using three distinct eddy diffusion profiles. Model 3 possesses turbopause altitudes of 840 km for methane and 760 km for molecular hydrogen. Meanwhile models 4 and 6 have turbopause altitudes of 940 km and 800 km for CH_4 and H_2, respectively. Last, model 5 exhibits the highest homopause altitudes of 980 km and 840 km for CH_4 and H_2.

Table 8. Arithmetic Percent Deviations Between the T-GITM Simulated Fields and the INMS Measurements of *Magee et al.* [2009][a]

	N_2 Density	CH_4 Density	H_2 Density	^{40}Ar Mixing Ratio	CH_4 Mixing Ratio	H_2 Mixing Ratio
Model 3	10.30	6.48	7.15	N/A	6.28	7.15
Model 4	9.56	5.61	5.66	12.20	6.49	7.05
Model 5	9.37	7.33	6.95	12.69	5.22	6.43
Model 6	10.02	6.71	5.82	12.25	8.40	7.01
Model 7	9.59	5.43	6.97	12.88	5.42	6.64
Model 8	9.12	6.54	6.40	12.13	6.36	7.38
Model 9	9.79	6.96	6.76	12.83	6.26	6.51
Model 10	9.57	5.22	6.65	N/A	6.34	6.67
Least Squares	7.31	4.74	4.99	7.12	4.86	4.77

[a]A least squares fit to the data is provided as a fiducial.

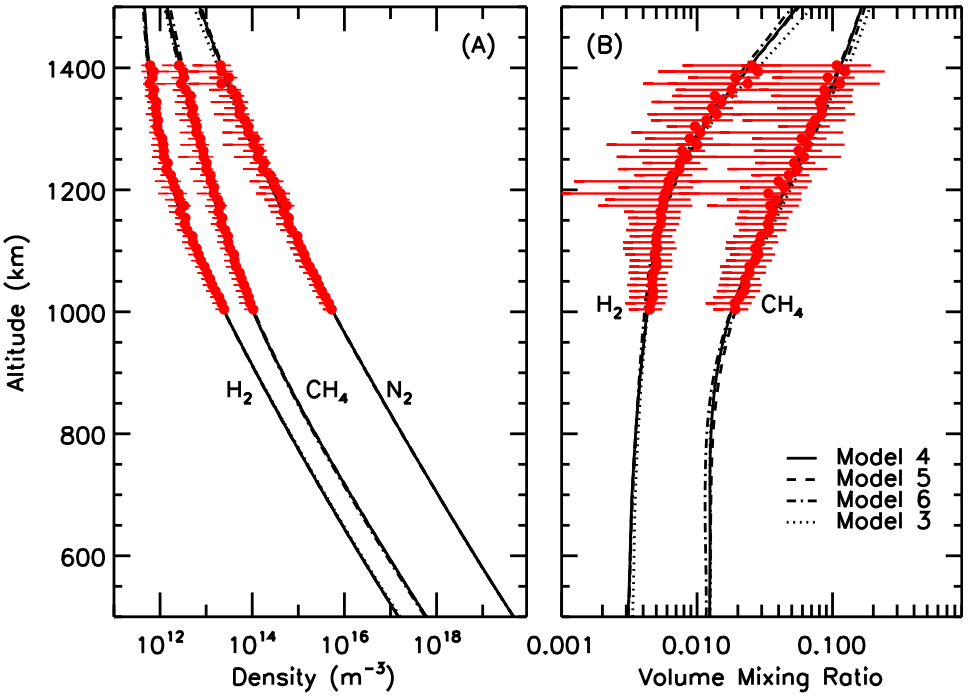

Figure 4. T-GITM simulated densities and mixing ratios (black lines) compared against the INMS data of *Magee et al.* [2009]. (a) The T-GITM simulated (black lines) and the INMS averaged neutral densities (red circles) of N_2, CH_4, and H_2. (b) The mixing ratio comparisons. Percentage deviations between the models and data are provided in Table 8. Horizontal red lines represent the variations due to the Cassini INMS trajectories and are not due to counting statistics.

[40] Figure 5c depicts the resulting ^{40}Ar volume mixing ratio profiles using these various eddy diffusion coefficients. First, we note that model 5 (LB Argon) possesses much lower Argon mixing ratios at the lowest altitudes, consistent with the reduction of the ^{40}Ar mixing ratios by 20% at 500 km. However, as can be seen in Figure 5c and in Table 8, models 4 (Magee), 5 (LB Argon), and 6 (Aerosols), all match the averaged Argon mixing ratios of *Magee et al.* [2009] (plotted in red) equivalently well. Also plotted in Figure 5c in blue are the approximate values of the Argon mixing ratios taken from *Yelle et al.* [2008]. Model 3 matches the blue argon data as well as the simulations of *Yelle et al.* [2008], as discussed in paper 1.

[41] Figure 5d contains the HCN volume mixing ratio profiles for these simulations. Model 3 possesses an artificial maximum allowable HCN mixing ratio enforced at 1.9×10^{-4}. Models 4 and 6 predict mixing ratios consistent with one another, due to their nearly identical eddy diffusion profiles. Model 5 simulates lower HCN mixing ratios than models 4 and 6, due to its greater turbulent coefficient seen in Figure 5b. The INMS-derived HCN volume mixing ratios from the method of *Magee et al.* [2009] are denoted by the red rectangle. Additionally, the simulated HCN abundance of *Vuitton et al.* [2006] is shown by the green diamond. Model 5 (LB Argon) best matches the range of INMS HCN mixing ratios reported between 1000 and 1100 km, while models 4 (Magee) and 6 (Aerosols) systematically overestimate the abundances in this altitude regime. Meanwhile model 3 (hydrodynamic) is artificially constrained to adopt an HCN mixing ratio profile that is roughly consistent with the photochemical modeling work of *Vuitton et al.* [2006], who reports a mixing ratio of 2.0×10^{-4} at 1100 km during the TA and T5 flybys.

3.1.1. Fluxes, Composition, and Aerosol Trapping

[42] Figures 6a and 6b contain the vertical velocities of CH_4 and H_2, respectively. Figures 6c and 6d contain the vertical fluxes of these same constituents in black, scaled so that they are all relative to the surface of Titan. In Figure 6c, the gray curve represents the vertical CH_4 fluxes from model 3(NC) in paper 1, which is identical to model 3 but excludes CH_4 chemical losses. The H_2 fluxes asymptote high in the atmosphere, indicating that they have reached a limiting value, which we interpret as its limiting flux [*Hunten*, 1973]. If we force the model to exceed this limiting flux at 1500 km, then the H_2 mixing ratio drops precipitously at the highest altitudes. This indicates that H_2 obtains ~99% of its limiting fluxes high in the atmosphere, which is also consistent with the findings by *Strobel* [2009] and *Cui et al.* [2008].

[43] Figure 7 depicts the mixing ratios of the key minor constituents for models 3–6. These mixing ratios can be directly compared to the composition produced by Scheme I in the work by *De La Haye et al.* [2008a]. Mixing ratios for H_2, CH_4, and ^{40}Ar are repeated here for completeness. Figure 7 illustrates two things: (1) the impacts of the chemistry in T-GITM and (2) the impacts of the vertical dynamics. The species H, C_2H_4, and H_2CN are particularly important to the formation of HCN and, therefore, they are critical to the Titan GITM. We also note that the T-GITM simulated C_2H_4 abundances are high relative to other more

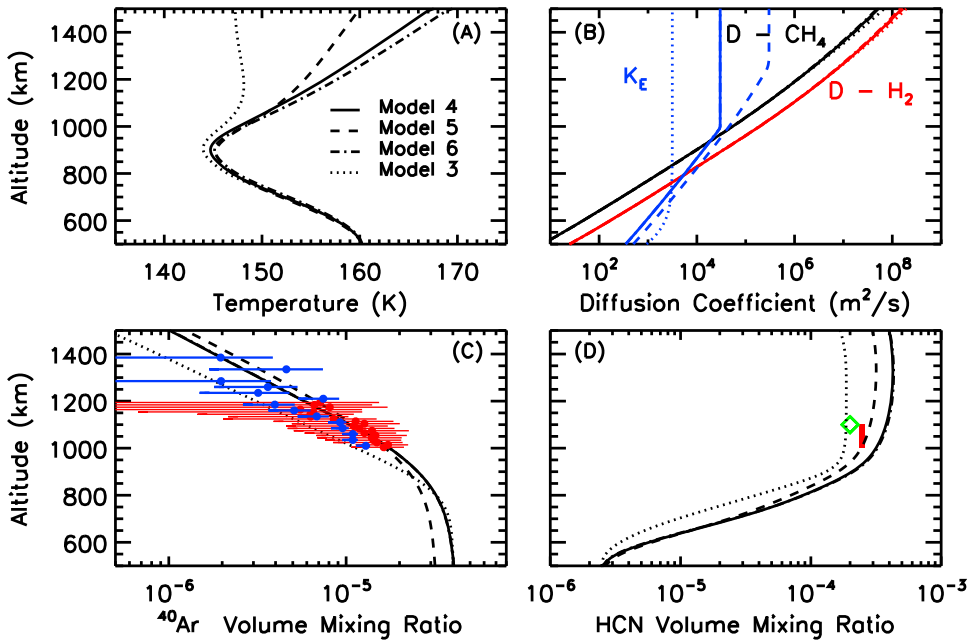

Figure 5. T-GITM simulated fields (black lines) and associated INMS measurements (when appropriate). Four models are shown, models 3, 4, 5, and 6 (see section 3.1 for details). (a) The temperatures (in K). (b) The eddy diffusion and molecular diffusion coefficients for CH_4 and H_2 (in $m^2\ s^{-1}$). (c) The simulated ^{40}Ar volume mixing ratios (black lines) compared against the data obtained by *Magee et al.* [2009] in red and that of *Yelle et al.* [2008] in blue. (d) The simulated HCN volume mixing ratio compared against the range of HCN values derived from the method of *Magee et al.* [2009] between 1000 and 1100 km (red rectangle) and against the chemical modeling of *Vuitton et al.* [2006] (green diamond). Please note that the results from models 4 and 6 are nearly coincident in Figure 5d, making them hard to distinguish from one another.

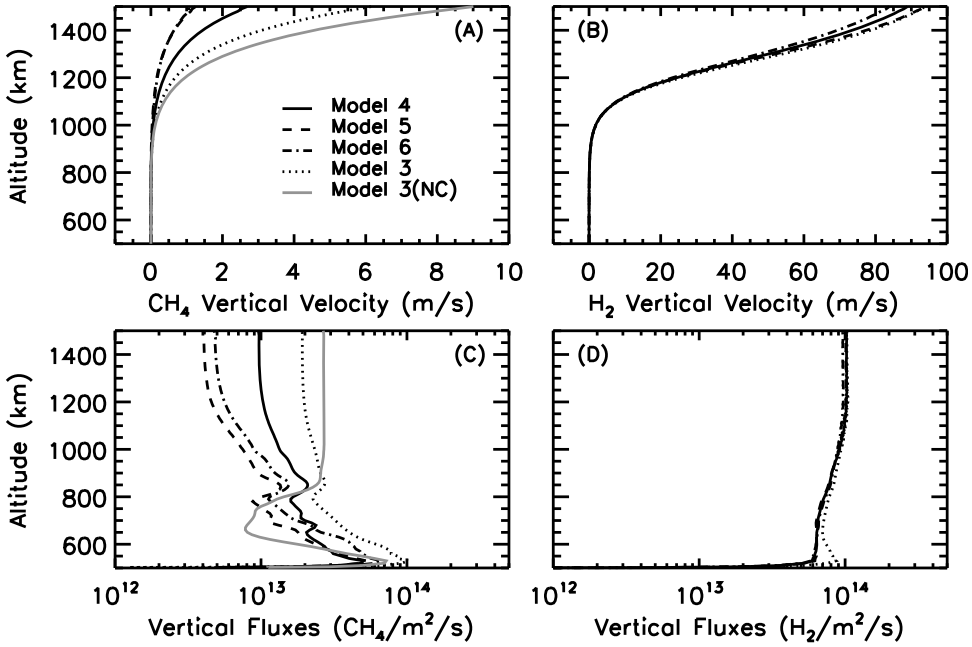

Figure 6. Simulated vertical speeds and fluxes for CH_4 and H_2. (a) Methane vertical velocities for each of the four models are compared. (b) Similar comparison of the vertical velocities for H_2. (c) The associated vertical methane fluxes throughout the atmosphere (in black). The grey line is model 3(NC) from paper 1, which does not include any CH_4 chemical losses. (d) The vertical fluxes of H_2 (in black), which obtains ~99% of its limiting flux above 1200 km.

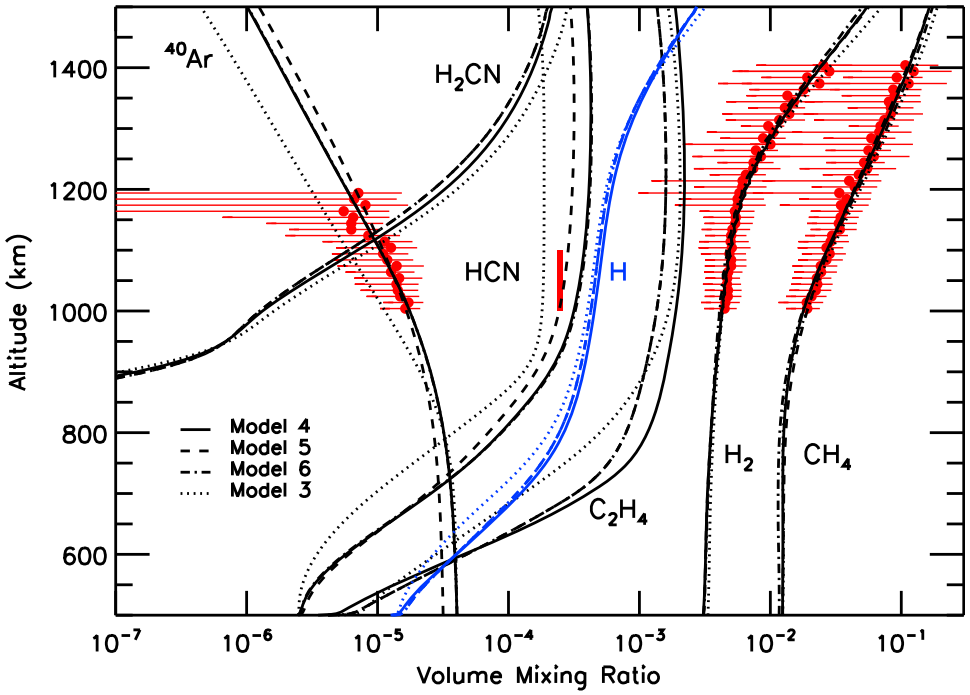

Figure 7. Simulated composition of key minor neutral species for models 3–6, illustrating the convolved effects of chemistry and dynamics. We note that models 4–6 are comparable in composition, but model 3 deviates significantly from the rest. This is most likely due to its much lower eddy diffusion coefficient, which results in higher abundances of some minor species. Also, we note that because C_2H_4 currently possesses no significant chemical losses in T-GITM, its mixing ratio is enhanced relative to that expected from other photochemical models. Averaged INMS data is overplotted in red for CH_4, H_2, HCN, and ^{40}Ar.

complete frameworks [e.g., *Krasnopolsky*, 2009], since we do not carry significant chemical losses for this species.

[44] In model 6, aerosol trapping is utilized as a loss process for all of the species listed in Table 1. The typical variation with altitude of this loss process is depicted in Figure 3, which contains the trapping rates of methane for this model. In model 6, the column-integrated trapping of CH_4, scaled relative to the surface of Titan, is equal to 3.20×10^{13} molecules m^{-2} s^{-1}. This value equals roughly one third of the total column-integrated loss of CH_4 due to chemistry [cf. *Mandt et al.*, 2009; *Krasnopolsky*, 2009].

3.1.2. Summary of Topside Escape Fluxes

[45] In this section, we have described 5 distinct T-GITM simulations and compared their simulated fields against the INMS data of *Magee et al.* [2009] with no scaling (see Table 7, left). Two cases, model 3 and model 3(NC), were taken directly from paper 1, each possessing the lowest methane homopause altitudes of 840 km (see Table 7). Model 3 represents the best proxy for *Strobel* [2009], requiring a topside flux of $\Phi_{CH_4} = 1.86 \times 10^{13}$ CH_4 m^{-2} s^{-1}. In model 3 (NC), after removing chemistry from model 3, the calculated methane fluxes required to match INMS rise to ~2.64×10^{13} CH_4 m^{-2} s^{-1}, as shown in Figure 6c by the solid gray curve. This agrees well with the work by *Yelle et al.* [2008], who also ignored chemistry and inferred topside escape fluxes of $2.5–3.0 \times 10^{13}$ CH_4 m^{-2} s^{-1}.

[46] Next, in model 4 (Magee), when the methane homopause rises to 940 km, the required methane fluxes needed to match INMS are reduced by nearly 50% to $\Phi_{CH_4} = 9.59 \times 10^{12}$ CH_4 m^{-2} s^{-1}. Then, in model 5 (LB Argon), the CH_4 homopause altitude is further increased to 980 km, which then subsequently reduces the required methane fluxes by an additional 58% to $\Phi_{CH_4} = 4.17 \times 10^{12}$ CH_4 m^{-2} s^{-1}. This increase in the homopause is accomplished by reducing the ^{40}Ar mixing ratios at 500 km by 20%. Finally, in model 6 (Aerosols) we reset the methane homopause altitude to 940 km and include aerosol trapping. The inclusion of aerosol trapping reduces the necessary methane topside escape rates relative to model 4 by ~50% to 4.85×10^{12}. Thus, the inclusion of aerosol trapping in model 6 is very similar to the impact of increasing the homopause altitude in model 5. The escape fluxes required by models 5 and 6 to match INMS are equivalent to a mass escape rate of $5.55 - 6.05 \times 10^{27}$ amu s^{-1}, which is consistent with the sputtering fluxes calculated from a kappa distribution by *De La Haye et al.* [2007a, 2007b] and *Johnson et al.* [2009]. However, as shown in Tables 6 and 7, every simulation matching the unscaled INMS densities of *Magee et al.* [2009] predicts topside CH_4 escape rates that are inconsistent with the most liberal upper limits imposed by CAPS and MIMI observations [*Crary et al.*, 2010; *Smith et al.*, 2009].

3.2. The 1-D T-GITM Compared With INMS Densities Scaled by a Factor of 3.0

[47] Despite altering the homopause altitudes and adding in aerosol trapping, we are not able to identify configurations of Titan GITM that match the unscaled INMS and that

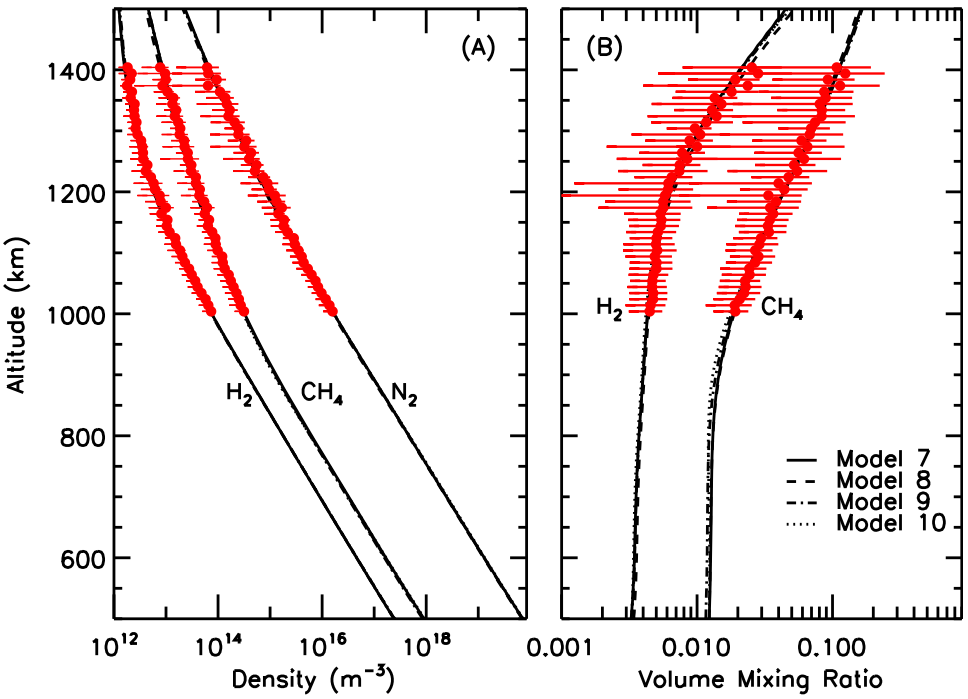

Figure 8. A comparison between T-GITM densities and mixing ratios (black lines) and the averaged INMS data scaled up by a uniform multiplicative factor of 3.0. (a) All four simulations are compared against the neutral densities (red circles) of N_2, CH_4, and H_2 derived from the method of *Magee et al.* [2009]. (b) The same simulations' volume mixing ratios for CH_4 and H_2 are compared against those derived from INMS. Percentage deviations between the models and data are provided in Table 8. Horizontal red lines represent the variations due to the Cassini INMS trajectories and are not due to counting statistics.

are consistent with CAPS and MIMI data. In this section, we show that by scaling up the INMS densities of *Magee et al.* [2009] by a uniform multiplicative factor of 3.0, we can simulate model configurations that are consistent with the INMS measurements and with the combined CAPS/MIMI observations. Additionally, we find that these configurations are also more consistent with measurements made by the HASI and the Composite Infrared Spectrometer (CIRS) investigations.

[48] In analogy with section 3.1, four simulations are now compared against the averaged INMS data of *Magee et al.* [2009] scaled by a uniform multiplicative factor of 3.0. We achieve this increase in densities at INMS altitudes self-consistently within T-GITM by increasing the total density at 500 km from 4.8×10^{19} up to 7.74×10^{19} m^{-3} and increasing temperatures from 160 to 180 K (see Table 5). These densities and temperatures are more consistent with those measured by the HASI [*Fulchignoni et al.*, 2005] at 500 km (see Figure 11). Moreover, they are also consistent with CIRS [*Achterberg et al.*, 2008]. The details of how we arrive at these lower boundary settings are given in paper 1.

[49] The four model runs of this section are labeled models 7, 8, 9, and 10 in Figures 8–10 and in Tables 5–7. These runs are intended to be analogues to the simulation suite in section 3.1. Model 10 now functions as the proxy for model 3 and, by extension, for the work by *Cui et al.* [2008], *Strobel* [2009], and *Yelle et al.* [2008]. Model 10 has the following settings: (1) an artificial maximum cap on HCN volume mixing ratio of 1.5×10^{-4}, (2) the eddy diffusion profile of *Yelle et al.* [2008], and (3) no external heating rates. Model 7 (scaled Magee) is now the analogue to model 4 (Magee). Model 8 (scaled LB Argon) is now the new version of the model 5 (LB Argon). Moreover, model 8 is identical to model 7, except it possesses a 15% reduction in its ^{40}Ar mixing ratios at 500 km. Last, model 9 (scaled Aerosol) is the new version of model 6 (Aerosol), and is identical to model 7, except it employs aerosol trapping. Table 7 summarizes how the different simulations of this section correspond to those of section 3.1.

[50] Models 7–9 employ the turbulent coefficient formulation given by *Atreya* [1986] and the full self-consistent chemistry of Figure 1 of paper 1. The external heating rates for models 7–10 vary from 0.0 (model 10) up to 115.0 eV cm^{-3} s^{-1} (models 7 and 9). The simulated major neutral densities from models 7, 8, 9, and 10 are shown in Figure 8, which is the same in construction as Figure 4. Table 8 contains the percentage deviation between these model simulations and the INMS data scaled up by a uniform factor of 3.0. Models 7, 8, 9, and 10 reproduce the scaled ingress INMS density measurements equivalently well.

[51] Figure 9 contains the same fields as in Figure 5. In Figure 9a, we note that the thermal structures for all of these simulations have shifted relative to their counterparts in Figure 5a, but exhibit the same general structures. Figure 9b depicts the location of the nominal homopause for both CH_4

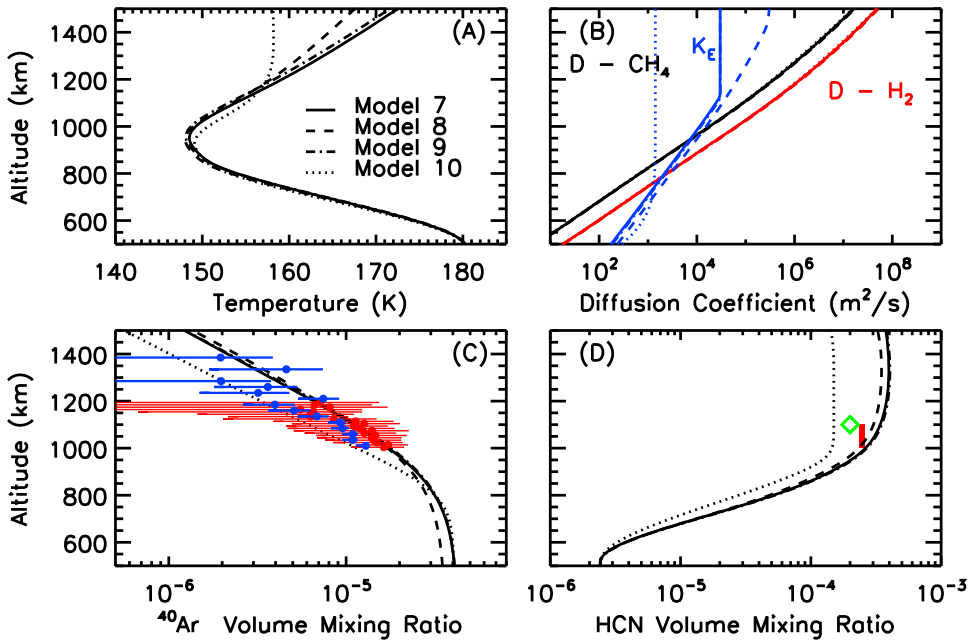

Figure 9. Key T-GITM simulated fields, organized identically to Figure 5 and depicting results from models 7–10 (see section 3.2). (a) The temperatures and (b) the eddy diffusion and molecular diffusion coefficients for CH_4 and H_2. (c) The simulated ^{40}Ar volume mixing ratios (black lines) compared against the data obtained by *Magee et al.* [2009] in red and that of *Yelle et al.* [2008] in blue. (d) The simulations' HCN volume mixing ratios (black) compared with the HCN mixing ratios derived from the INMS data of *Magee et al.* [2009] (red rectangle) and 0-D modeling by *Vuitton et al.* [2006] (green diamond). Note that in Figure 9d, results from models 7 and 9 are nearly coincident.

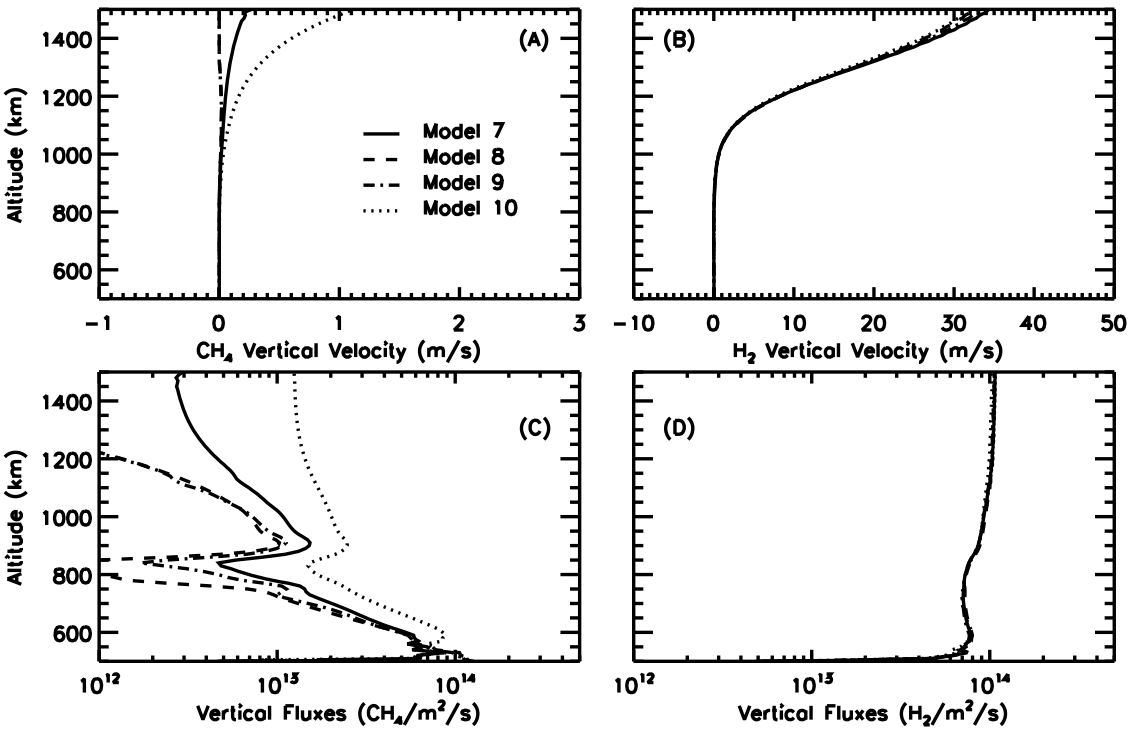

Figure 10. Vertical velocities and fluxes for CH_4 and H_2 in models 7–10. (a) Methane vertical velocities for the four models are compared. (b) Similar comparison of the vertical velocities for H_2. (c) The vertical methane fluxes throughout the atmosphere. (d) The vertical fluxes of H_2 which reach roughly 99% of its limiting flux above 1200 km.

and H_2. The magnitude of these molecular and eddy diffusion coefficients are reduced relative to those in section 3.1. This reduction occurs primarily due to the increased neutral densities of this simulation set.

[52] Model 10 has turbopause altitudes of approximately 850 km for methane and 770 km for molecular hydrogen. Meanwhile, models 7 and 9 possess higher turbopause altitudes of 950 km and 790 km for CH_4 and H_2, respectively. Last, model 8 has the highest homopause altitudes of 990 km and 830 km for CH_4 and H_2. Despite minor differences, these simulations' homopause altitudes remain consistent with their counterparts in section 3.1 (see, for example, Table 7).

[53] Figure 9c depicts the resulting ^{40}Ar volume mixing ratios, and it is nearly identical to Figure 5c. However, now model 8 employs ^{40}Ar mixing ratios reduced by 15% at 500 km (see Table 5). Please note that this is different from section 3.1, where we reduced the ^{40}Ar mixing ratio by 20% in model 5 (Table 5 contains the exact values). Figure 9d contains the HCN volume mixing ratio profiles for these four simulations and is similar to Figure 5d. As in section 3.1, we find that the simulation possessing the highest homopause altitude (model 8) best matches the measured HCN abundances of *Magee et al.* [2009] and the modeling result from *Vuitton et al.* [2006].

3.2.1. Vertical Fluxes and Aerosol Trapping

[54] Figure 10 contains the vertical velocities and fluxes of CH_4 and of H_2, and it is identical in construction to Figure 6. However, the vertical velocities of CH_4 and H_2 are significantly reduced in this configuration relative to their counterparts in section 3.1. In fact, as can be seen in Figure 10c, the vertical methane fluxes calculated by models 8 and 9 drop precipitously in the highest altitudes. As in section 3.1, the H_2 fluxes reach ~99% of their limiting flux high in the atmosphere. However, unlike section 3.1, the vertical velocities of H_2 required to match the scaled INMS data are less than the full thermal Jeans Escape velocity at 1500 km, which is ~45 m s^{-1}.

[55] Model 9 incorporates aerosol trapping as a loss process for key species, as model 6 does in section 3.1. The altitude cutoff for the aerosol trapping was increased from 625 km up to 700 km, which is still consistent with the hardening of the aerosols described by *Bar-Nun et al.* [2008]. We adjust the cutoff altitude in order to reduce the column-integrated trapping of CH_4, scaled relative to the surface of Titan, to 6.97×10^{12} molecules m^{-2} s^{-1}. This updated microphysical loss rate is equivalent to between ~5–10% of the total column-integrated loss of methane due to chemistry [see *Krasnopolsky*, 2009; *Mandt et al.*, 2009]. Moreover, we note that this calculated column-integrated aerosol trapping is significantly reduced relative to that reported in section 3.1.

3.2.2. Topside Escape Fluxes

[56] When constrained to match the scaled average ingress INMS data of *Magee et al.* [2009], model 7 (scaled Magee) requires significantly reduced escape fluxes when compared with any of the simulations either in section 3.1 or in paper 1. This model requires a topside escape flux for CH_4 of $\Phi_{CH_4} = 3.24 \times 10^{12}$ molecules m^{-2} s^{-1} referred to the surface (4.31×10^{27} amu s^{-1}). This escape flux is consistent with the sputtering fluxes derived from a kappa distribution by *De La Haye et al.* [2007b]. When a column-integrated aerosol trapping of 6.97×10^{12} CH_4 m^{-2} s^{-1} is included in model 9, there is effectively no escape of CH_4 ($<10^8$ molecules m^{-2} s^{-1}) needed to match the scaled average INMS CH_4 densities and mixing ratios. Similarly, in model 8 (scaled LB Argon), negligible escape fluxes of CH_4 ($<10^8$ molecules m^{-2} s^{-1}) are needed to explain the scaled average INMS data. Last, model 10 possesses the highest outflow rates of this section, requiring $\Phi_{CH_4} = 1.25 \times 10^{13}$ molecules m^{-2} s^{-1}. These results are summarized in Table 7 and directly compared with the results in section 3.1.

4. Discussion and Analysis

[57] In order to investigate the dynamics, composition, and energetics of Titan's upper atmosphere, we have presented a series of distinct 1-D T-GITM simulations that are constrained to match the average ingress INMS data of *Magee et al.* [2009], both unscaled and scaled by a factor of 3.0. Table 8 demonstrates that all models match the INMS data (scaled and unscaled) equivalently well in all of the major densities and mixing ratios. This study suggests that, within the limited constraints imposed by the available data and its associated uncertainties, an entire spectrum of atmospheric configurations can reproduce the INMS composition measurements, based upon on their "goodness of fit." Next, we outline the major results of this study and some potential limitations of the work presented here.

4.1. Potential Impacts of Aerosol Trapping

[58] The first observation from our investigations is that aerosol trapping can have a significant impact on both the mass balance of the upper atmosphere and on the available methane escape flux at 1500 km (cf. sections 3.1 and 3.2). This is true even though T-GITM utilizes conservative values for the aerosol trapping efficiences. In model 6, the column-integrated aerosol trapping rates of methane amount to 3.2×10^{13} CH_4 m^{-2} s^{-1} (referred to the surface), which represents roughly 30% of the column-integrated chemical destruction rate of methane [*Krasnopolsky*, 2009]. Using this additional mass loss, the escape rates of CH_4 required to reproduce the INMS measurements are reduced by 49% relative to model 4 and by 74% relative to the hydrodynamic case (model 3). In model 9, the column-integrated aerosol trapping rates are calculated to be 6.97×10^{12} molecules m^{-2} s^{-1}. This amount of aerosol trapping reduces the simulated topside methane escape fluxes by more than 99%.

[59] The potential impacts of aerosol trapping identified here corroborate similar findings by *Liang et al.* [2007]. In that work, the authors introduced an aerosol adsorption mechanism, whereby atmospheric constituents were removed by ambient aerosols, which were derived from measurements made by the Ultraviolet Interferometer Spectrometer (UVIS) [*Shemansky et al.*, 2005]. *Liang et al.* [2007] found that, using conservative adsorption rates and measured aerosol abundances, they simulated configurations of Titan's upper atmosphere that required a net influx of

methane material from the magnetosphere. In many ways their investigation anticipated the results that we have presented, except, instead of basing our aerosol abundances upon UVIS direct measurements, we have employed the work by *Bar-Nun et al.* [2008] and the experimental trapping rates by *Jacovi and Bar-Nun* [2008]. Despite these differences, both studies employed very similar physicochemical mechanisms and they have shown that aerosols can have an important impact upon the mass balance of the methane in the upper atmosphere.

[60] However, the fundamental question emerges, "Are the aerosol trapping rates of this investigation reasonable?" Depending on the simulation (model 6 or model 9), the column-integrated aerosol trapping rates in this work range between 5 and 30% of the total column-integrated chemical destruction of CH_4. This additional mass loss lies within the range of uncertainties in current estimates for the total chemical destruction of methane [*Mandt et al.*, 2009]. Thus, in a simple order-of-magnitude sense, this additional physicochemical loss of methane to the aerosols is reasonable. Or, more to the point, these rates do not seem particularly unreasonable given the uncertainties surrounding our current knowledge of the chemistry occurring in Titan's upper atmosphere.

[61] Thus, aerosol trapping, as it is currently implemented in T-GITM, represents a significant component in the mass balance of Titan's atmosphere, and it suggests the existence of a ground-to-exosphere hygrological cycle of methane. Recent work by *Atreya et al.* [2006] posits the presence of a methane analogue to Earth's hydrological cycle in Titan's lower atmosphere. Meanwhile, the work by *Lorenz et al.* [2008] indicates that the dunes covering a substantial amount (up to 20%) of the moon's surface area are composed of aerosol material. Taken together, these two works indicate that (1) material may cycle from the surface to the atmosphere and back to the surface and (2) that a significant deposition of aerosols onto the surface is most likely occurring. The aerosol trapping mechanism presented here might represent another link in this cycle. For instance, if these aerosol cages are transporting methane (recycling the atmospheric methane) back to the surface, then perhaps there is a process that would eventually release the trapped gases over geologic timescales. This process could supply some of the methane that is currently required by photochemical models [e.g., *Krasnopolsky*, 2009] from subsurface sources.

4.2. A New Perspective on Topside Mass Loss Processes

[62] One of the more significant results from the modeling studies of *Strobel* [2008, 2009] and *Yelle et al.* [2008] is that the relatively heavy constituent, CH_4, is suggested to escape at very large rates globally from Titan (between 44 and 66 kg s^{-1}). Moreover, this escape is posited to be driven by thermal escape of the atmosphere, through a mechanism termed by *Strobel* [2008] as "slow, dense hydrodynamic escape." Hydrodynamic outflow is suggested to have occurred in planetary atmospheres early in their formation [cf. *Tian et al.*, 2008], whereby the outward flow of material would adiabatically cool the upper thermosphere. This adiabatic cooling provides stability to nascent atmospheres by preventing the onset of atmospheric blow off. In Titan's present thermosphere, *Strobel* [2009] posits that hydrodynamic escape preferentially removes CH_4, leaving N_2 largely unaffected by this outflow. Contrary to this hypothesis, experimental evidence from CAPS IMS and MIMI CHEMS indicates that these high outflows of CH_4 are not likely [see *Crary et al.*, 2009; *Sittler et al.*, 2008; *Smith et al.*, 2009]. Also, as pointed out by *Johnson et al.* [2009] and *Tucker and Johnson* [2009], the methane escape predicted by the hydrodynamic outflow model is inconsistent with monte carlo simulations of the exosphere.

4.2.1. CH_4 Escape From Titan

[63] This investigation utilizes the significant uncertainties in Titan's atmosphere between 500 km and 1000 km in order to ask the basic question, "Can we reproduce INMS measurements in the thermosphere, while still using CH_4 escape rates consistent with CAPS and MIMI?" In doing so, we have illustrated that, in fact, a broad range of CH_4 escape fluxes from Titan's upper atmosphere can reproduce the INMS measurements determined by *Magee et al.* [2009] equally well. We have summarized the most salient results in Table 7.

[64] The first and perhaps the most prominent determinant for the required topside CH_4 escape fluxes needed to match INMS composition is whether or not one chooses to match the unscaled or scaled INMS data. A systematic trend is observed by comparing model 3 to model 10, model 4 to model 7, model 5 to model 8, and model 6 to model 9. In each case, the simulated topside escape fluxes for CH_4 are dramatically reduced in those simulations matching the scaled INMS densities relative to their counterparts matching the unscaled INMS densities. The reason for this difference is manifold. First, increasing the total densities in the scaled cases results in an enhancement in the chemical destruction of CH_4. Second, the momentum coupling between N_2 and CH_4 is enhanced in the cases matching the INMS densities scaled up by a factor of 3.0. Both processes have the net effect of reducing the upward flux of methane. In a future paper, we outline in detail how these different processes impact the simulations.

[65] The second major determinant for the methane fluxes, the CH_4 homopause altitudes, is relatively elementary and is already well documented by *Yelle et al.* [2006]. After selecting simulations that match either the scaled INMS or the unscaled INMS, one observes in Table 7 that the required CH_4 fluxes vary inversely with the adopted homopause altitude. In other words, as the homopause altitude increases, the required CH_4 escape fluxes decrease. This is consistent with the results found by *Yelle et al.* [2006], who report a similar correlation between the eddy diffusion coefficient and the topside methane fluxes required to match the INMS data.

[66] The third major determinant for our estimates of methane escape is the inclusion of aerosol trapping. Two models, model 6 and model 9, include this physicochemical process and they show that the inclusion of aerosol trapping mimics the effect of a higher homopause. This result is also straightforward to explain. As the column-integrated trapping rates increase, there is less methane material left to escape from the topside of Titan.

[67] From the results in sections 3.1 and 3.2 (see Table 7), we can make some additional observations. First, when

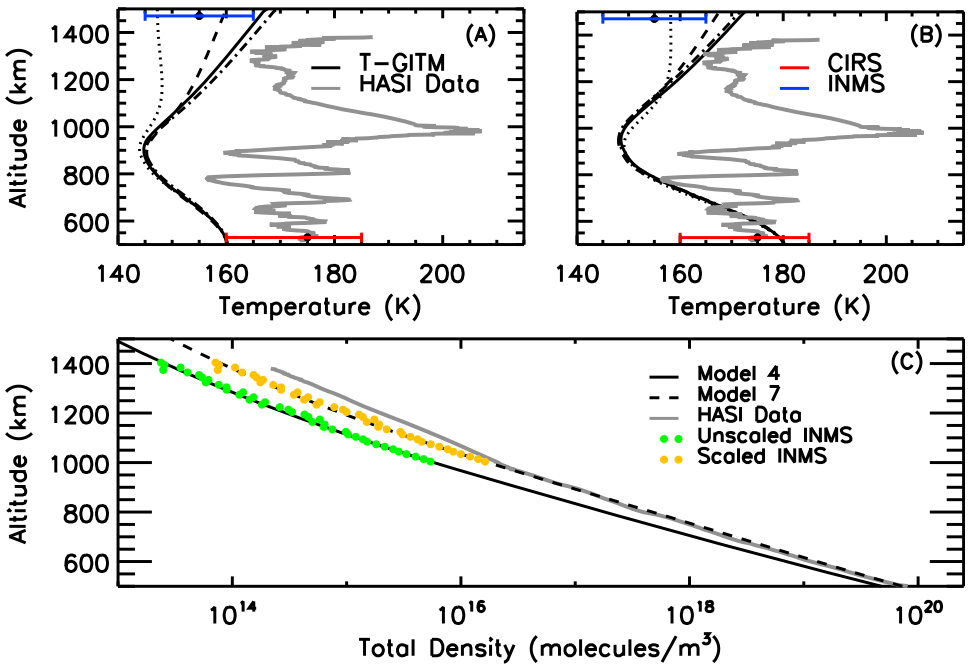

Figure 11. T-GITM simulated temperatures and total neutral densities compared against CIRS and HASI data. (a) Comparison of the thermal structures (black lines) of the model simulations matching the unscaled INMS densities (section 3.1) with the HASI temperatures (grey lines). Overplotted is also the CIRS measurements near 500 km (red horizontal range) and the inferred temperatures at the exobase of *Müller-Wodarg et al.* [2008] as blue horizontal lines. (b) The same information for the simulations matching the scaled INMS densities (see section 3.2). (c) Comparison of the total neutral densities of T-GITM (black lines) in models 4 and 7 versus the HASI neutral densities (grey lines). Also plotted are the unscaled INMS total densities of *Magee et al.* [2009] (green circles) and the scaled densities (yellow circles).

matching the ^{40}Ar mixing ratios of *Yelle et al.* [2008], which enforces a lower homopause of 840.0 km on methane, T-GITM requires hydrodynamic-like fluxes. This result is independent of whether or not we match the unscaled or the scaled INMS densities (compare models 3, 3(NC), or 10). These fluxes range from 1.25×10^{13} (model 10) up to 1.86×10^{13} CH_4 m^{-2} s^{-1} (model 3) and, if we ignore chemistry, up to 2.64×10^{13} CH_4 m^{-2} s^{-1} in model 3(NC). The fluxes of model 10 are less than those reported by either *Strobel* [2009] or *Yelle et al.* [2008], but they are still consistent with hydrodynamic-like escape fluxes. Thus, we conclude that enforcing the homopause altitude of 840 km on methane requires high escape rates of CH_4 in order to match the INMS composition, regardless of any other parameter settings.

[68] If we instead relax this condition, and constrain the T-GITM to match the range of ^{40}Ar mixing ratios derived by *Magee et al.* [2009], then the model identifies a spectrum of topside methane escape rates that reproduce the INMS composition (scaled and unscaled) equally well. These varying escape regimes can be described best as (1) enhanced thermal escape (model 4) or (2) sputtering/nonthermal escape (models 5, 6, and 7) consistent with that posited by *De La Haye et al.* [2007a, 2007b] and *Johnson et al.* [2009]. The escape fluxes in these regimes range from 4.17×10^{12} up to 9.59×10^{12} CH_4 m^{-2} s^{-1}. The lowest escape fluxes occur when we reduce the lower boundary mixing ratios of ^{40}Ar by 20% (model 5) or when we add a column-integrated aerosol trapping rate of 3.2×10^{13} CH_4 m^{-2} s^{-1} (model 6).

[69] Finally, when we constrain the Titan model to match the range of ^{40}Ar mixing ratios of *Magee et al.* [2009] and the INMS densities scaled by a factor of 3.0, then we can reproduce the INMS CH_4 densities and mixing ratios with negligible escape of methane. This is done in both models 8 and 9. In model 8, we reduce the Argon mixing ratios by 15% at 500 km, which imposes a higher homopause altitude of 990 km on methane. In model 9, we impose a methane homopause altitude of 940 km, but also include a column-integrated aerosol trapping rate of 6.97×10^{12} molecules m^{-2} s^{-1}, which reduces the topside escape to essentially zero. These last two configurations are the only simulations of this study that are consistent with both INMS measurements and with observations made by CAPS and MIMI.

4.2.2. CH_4 Escape Speeds: Are They Realistic?

[70] Having summarized the different methane escape flux regimes required by T-GITM to reproduce the INMS densities, we next address whether or not the model simulates these rates self-consistently. For all simulations, except models 8 and 9, the escape velocities for CH_4 must be imposed upon the model at 1500 km. Models 5, 6, and 7 all represent topside escape rates of CH_4 consistent with nonthermal sputtering fluxes [*Johnson et al.*, 2009]. Because a fluid model cannot capture this process self-consistently, T-GITM requires the specification of these vertical velocities consistent with nonthermal mechanisms at 1500 km. The same is true for models 3, 3(NC), and 10, but, in these

cases, this lack of self-consistency poses a more significant problem.

[71] As discussed in paper 1, the hydrodynamic fluxes consistent with *Strobel* [2009] and *Yelle et al.* [2008] are posited to be driven from below by an excess in available energy from solar EUV/UV heating that is transported upward by thermal conduction. Despite accounting for both of these physical processes in models 3, 3(NC), and 10, T-GITM still cannot reproduce hydrodynamic escape self-consistently. Instead, this escape must be imposed on the upper boundary. This suggests that, regardless of the model configuration, the escape fluxes consistent with hydrodynamic escape rates may be driven by mechanisms outside the 1-D model, such as either global transport or external, nonthermal processes, as suggested by *Tucker and Johnson* [2009] and *Johnson et al.* [2009].

[72] On the other hand, the models possessing the lowest escape rates (models 8 and 9) calculate CH_4 escape self-consistently, meaning that the physics of the Navier-Stokes equations are sufficient. There is no need to impose escape speeds at 1500 km (see Table 6). Instead, we impose the boundary condition of $\frac{\partial v_s}{\partial r} = 0.0$, where v_s is the vertical velocity of species "s" and r is radius. This boundary condition means that the velocities calculated by the physical domain determine the escape rates. This is in contrast to simulations where we specify an escape velocity that then overrides the physical calculations of the Navier-Stokes model.

4.2.3. Escape of Molecular Hydrogen

[73] As discussed in the previous section, the required methane escape fluxes vary widely among the different model simulations. By contrast, all simulations require topside escape fluxes of H_2 within a very tight range of $9.67 \times 10^{13} - 1.07 \times 10^{14}$ molecules m^{-2} s^{-1}. Moreover, these fluxes are consistent with those calculated by *Cui et al.* [2008] and *Strobel* [2009]. In all of the simulations, the H_2 escape fluxes are determined by the combination of its photochemical production and its limiting fluxes that are established deep in the atmosphere [*Hunten*, 1973].

[74] Most significantly, the primary differences between the models center around the actual escape speeds of H_2. When comparing model results against the unscaled INMS densities, molecular hydrogen must achieve velocities of roughly 90–100 m s^{-1} (see Figure 6), which are in excess of the thermal escape speeds predicted by Jeans escape (45 m s^{-1}). Thus, a mechanism must be posited to accelerate them, because these escape velocities are (1) not self-consistently calculated and (2) not consistent with classical theory. As discussed in paper 1, *Cui et al.* [2009] suggests that collision-dominated 13-moment corrections (i.e., Navier-Stokes corrections) to the Velocity Distribution Function (VDF) may account for this enhanced thermal escape self-consistently.

[75] On the other hand, when comparing model results against the scaled INMS densities (section 3.2 and Figure 10), H_2 only requires topside escape velocities of ~35 m s^{-1}, which is easily provided by classical thermal escape mechanisms. T-GITM can self-consistently calculate the H_2 escape speeds without relying upon additional enhancements to the thermal escape.

[76] This difference between the unscaled and scaled cases points out an interesting difference in the interpretation of H_2 escape, as described by *Hunten* [1973]. When matching the unscaled INMS densities, the limiting flux of H_2 is so large relative to the classical Jeans escape flux that we must find an additional driver to enhance thermal escape at 1500 km. This indicates that the topside escape rates are determined by the availability of energy at the exobase. When matching the scaled INMS densities, the available thermal energy at the exobase is more than sufficient to accommodate the upwelling fluxes from below. In this latter scenario, the H_2 escape is limited from deep within the atmosphere, in analogy with Earth, where the exospheric temperature is high enough that the outflow of H_2 is determined by the limiting flux from deep in the atmosphere and not by the available thermal escape at the exobase.

4.3. Reconciling T-GITM With HASI, GCMS, CIRS, INMS, MIMI, and CAPS

[77] Throughout this investigation, we focus on simulating configurations of Titan's upper atmosphere consistent with the INMS neutral densities and mixing ratios of *Magee et al.* [2009], in order to quantify the range of CH_4 escape rates possible within these constraints. As shown in Tables 4 and 5, the models' lower boundary settings are constrained to match the Huygens Gas Chromatograph Mass Spectrometer (GCMS) and Cassini CIRS [*Niemann et al.*, 2005; *Achterberg et al.*, 2008]. Table 8 contains the quantitative comparison between INMS and the T-GITM simulations. Moreover, Table 6 presents a direct comparison between T-GITM's required methane escape fluxes and the upper limits established by the combined CAPS and MIMI observations.

[78] Next, we evaluate how the T-GITM simulations compare with the other observations of Titan's atmosphere made by CIRS and by HASI [*Achterberg et al.*, 2008; *Flasar et al.*, 2005; *Fulchignoni et al.*, 2005]. In Figure 11, we present simulated thermal and density structures compared against 3 separate Cassini-Huygens investigations. There are several key items to note from Figures 11a–11c. First, in Figure 11b, models 7–10 match the CIRS and HASI temperatures at low altitudes, although they do not match the HASI temperatures at altitudes above 800 km [*Achterberg et al.*, 2008; *Fulchignoni et al.*, 2005]. Second, in Figure 11a, the unscaled simulations, by contrast, do not compare favorably with HASI at any altitude and match only the coldest temperatures measured by CIRS at 500 km. Finally, in Figure 11c, the simulations matching the scaled INMS densities (model 7) do a much better job reproducing the HASI densities below 1000 km than the simulations matching the unscaled INMS densities (model 4).

[79] Hence, out of models 3–10, we conclude that the simulations matching the scaled INMS densities better match the temperatures measured by CIRS at 500 km. Moreover, these same simulations (models 7–10) also better correlate with HASI densities and temperatures. Thus, these simulations reconcile measurements from INMS, HASI, and CIRS into a single, coherent configuration. Furthermore, as shown in Table 6, models 8 and 9 also calculate CH_4 topside escape fluxes consistent with both CAPS and MIMI. As discussed earlier, the CAPS IMS instrument has placed liberal upper limits to the methane mass escape at roughly 1.0×10^{26} amu s^{-1} globally. Similarly, the MIMI CHEMS investigation finds that the ionic carbon material surrounding the moon amounts to only 1.3% of the ionic oxygen

material [*Smith et al.*, 2009]. The authors indicate that this result is consistent with the CAPS IMS investigation of *Crary et al.* [2009].

[80] Therefore, we conclude, based upon these considerations of this section, that models 8 and 9 represent the optimal configurations of any simulation presented here (models 3–10). Models 8 and 9 simulate densities, mixing ratios, temperatures, and escape rates that are consistent with HASI, GCMS, INMS, CIRS, MIMI, and CAPS. This means that these two simulations are consistent with six separate investigations of Titan's upper atmosphere and its magnetospheric environment, making these configurations the most compelling representations of Titan's thermosphere in the present study.

4.4. HCN: Another Possible Constraint on K_E

[81] In *Bell et al.* [2010] (paper 1), we found that quantifying the feedbacks between the dynamics, chemistry, and energetics of Titan's upper atmosphere is critical to understanding the physics determining the composition measurements of INMS. The results presented in this investigation back up the findings from paper 1. Inspecting both Figures 5d and 9d, we note that the asymptotic abundance of HCN at high altitudes is systematically reduced as the homopause altitude increases. However, even when using the highest homopause altitudes of models 5 and 8, T-GITM still overestimates the HCN mixing ratios relative to either the data reduction from INMS [*Magee et al.*, 2009] or the simulations of *Vuitton et al.* [2006]. Thus, based solely upon the HCN abundance comparison, it appears that a homopause altitude for methane higher than 1000 km may be required.

[82] Of course, an equally valid alternative is that more chemical losses of HCN are necessary. However, when comparing T-GITM simulated HCN mixing ratios in Figures 5d and 9d to those simulated by *Krasnopolsky* [2009] (who possessed a significantly more sophisticated scheme than that employed here), one notes that including more chemistry may potentially increase the HCN abundances at INMS altitudes. Thus, in order to decrease the HCN abundances at high altitudes, we must posit either (1) a higher homopause than any considered here or (2) an additional loss (chemical or heterogenous) for HCN in T-GITM. Assuming that the Titan model captures the most salient chemical losses in Scheme I of *Bell et al.* [2010], then additional losses of HCN can be introduced by increasing aerosol trapping of HCN. This increase in aerosol trapping can be obtained by increasing the HCN aerosol trapping efficiency from the very conservative 1% shown in Table 1. Experimentally, it is shown that HCN, due to its strong dipole moment, is very easily trapped in amorphous water ice [*Notesco and Bar-Nun*, 1997]. Thus, an increase in aerosol trapping of HCN appears to be warranted, based upon experimental measurements of HCN trapping in water ice.

4.5. Summary of Key Results From This Work

[83] 1. The homopause established by the ^{40}Ar mixing ratios from *Yelle et al.* [2008] requires high CH_4 escape, regardless of other parameters. When constrained to match the ^{40}Ar mixing ratios of *Yelle et al.* [2008] a homopause altitude of 840 km is imposed upon methane. Using these settings, hydrodynamic escape of CH_4 is required, regardless of other parameters, with escape fluxes ranging from 1.25×10^{13} (model 10) up to 2.64×10^{13} (model 3(NC)). This high outflow cannot be self-consistently calculated, leading us to conclude that this escape, if present, may be driven by either global transport or by external mechanisms, as suggested by *Tucker and Johnson* [2009]. Finally, this outflow is inconsistent with the observations made by CAPS and MIMI in the Saturnian magnetosphere near Titan.

[84] 2. When constrained to match the ^{40}Ar mixing ratios of *Magee et al.* [2009], an entire range of possible escape scenarios emerges. The CH_4 escape regimes break down into roughly 3 scenarios: (1) enhanced thermal escape of model 4 ($\sim 9.59 \times 10^{12}$ CH_4 m^{-2} s^{-1}), (2) sputtering and nonthermal escape in models 5, 6, and 7 ($3.24 - 4.85 \times 10^{12}$ CH_4 m^{-2} s^{-1}), and (3) negligible escape in models 8 and 9. Models 8 and 9 reproduce INMS with high accuracy and predict CH_4 escape rates consistent with CAPS and MIMI observations. Finally, the velocities for the enhanced thermal escape and the nonthermal escape scenarios must be imposed on the calculation domain and are not self-consistently calculated by the model, just as in the case of hydrodynamic escape.

[85] 3. Scaling the INMS densities by a factor of 3.0 results in significant differences in estimated methane escape rates in T-GITM. In general, for any given set of parameters, T-GITM requires systematically lower CH_4 escape fluxes to match the INMS densities of *Magee et al.* [2009] when scaled by a factor of 3.0 relative to the fluxes required when matching the unscaled INMS densities. This is shown directly in Table 7.

[86] 4. Scaling INMS densities by a factor of 3.0 makes the resulting simulations consistent with six separate investigations: INMS, HASI, GCMS, CIRS, CAPS, and MIMI. When matching the INMS neutral densities scaled by a factor of 3.0, T-GITM can simulate atmospheric configurations that are simultaneously consistent with CIRS temperatures at 500 km, HASI temperatures below 800 km, HASI densities below 1000 km, INMS densities above 1000 km, and GCMS composition at 500 km (as boundary conditions). Finally, two simulations, models 8 and 9, require topside methane escape consistent with the upper limits inferred by CAPS and MIMI (~ 1.0 1.0×10^{26} amu s^{-1}). Figure 11 gives an overview of T-GITM's consistency with these six investigations.

[87] 5. T-GITM calculated aerosol trapping rates have important implications for the mass balance of the thermosphere. Using the aerosol embryo densities from *Bar-Nun et al.* [2008] combined with conservative aerosol trapping efficiencies, we find that the physicochemical process of aerosol trapping represents a potentially significant component to the mass balance of CH_4. This process may provide a critical link between the upper and lower atmospheres by trapping gaseous molecules and transporting them downward from the thermosphere. Moreover, our results with aerosol trapping are similar to those of *Liang et al.* [2007].

[88] 6. H_2 escape fluxes are consistent among all simulations. The H_2 topside escape fluxes for all of the simulated configurations range between 9.67×10^{13} and 1.08×10^{14} molecules m^{-2} s^{-1}, with vertical velocities ranging from 35 m s^{-1} (75% of Jeans escape) to 100 m s^{-1} ($\sim$ 200% Jeans

escape). In all cases, H_2 achieves ~99% of its limiting flux [*Hunten*, 1973], which is consistent with *Strobel* [2009] and *Cui et al.* [2009].

[89] 7. Measured abundances of HCN imply a methane homopause greater than those considered here, or additional losses to chemistry/aerosols. The calculated HCN mixing ratios, using the chemical scheme of *Bell et al.* [2010, Figure 1], best match the data of *Magee et al.* [2009] when using the highest methane homopause altitudes of 960–990 km. However, these simulations still overestimate the measured HCN abundances, implying a higher homopause or additional chemical or aerosol losses of HCN. Moreover, the photochemical modeling results of *Vuitton et al.* [2006] argue for an even higher homopause altitude and/or higher aerosol trapping.

[90] 8. T-GITM simulations that require hydrodynamic methane fluxes consistent with *Strobel* [2009] and *Yelle et al.* [2008] possess several key limitations. First and foremost, a mechanism must be posited to eliminate roughly 99% of this escaping neutral methane in order to explain the ion measurements in the near-Titan magnetosphere by CAPS and MIMI [see *Crary et al.*, 2009]. Moreover, these high escape fluxes cannot be reproduced by the nonhydrostatic Navier-Stokes model self-consistently. Instead, these escape rates are enforced as boundary conditions and actually override the physics of the model itself. For these reasons, the simulations that produce the hydrodynamic CH_4 escape fluxes remain highly speculative. Moreover, as we have shown, given the uncertainties surrounding our knowledge of Titan's upper atmosphere these configurations are not unique, and there exist multiple examples of T-GITM simulations that can reproduce INMS densities and mixing ratios while calculating *self-consistently* low methane escape rates in line with CAPS and MIMI.

[91] **Acknowledgment.** The authors would like to acknowledge funding from NASA grant NAS703001NM0710023, subcontracted through the Jet Propulsion Laboratory (JPL).

References

Achterberg, R. K., B. J. Conrath, P. J. Gierasch, F. M. Flasar, and C. A. Nixon (2008), Titan's middle-atmospheric temperatures and dynamics observed by the Cassini Composite Infrared Spectrometer, *Icarus*, *194*, 263–277, doi:10.1016/j.icarus.2007.09.029.

Atreya, S. K. (1986), *Atmospheres and Ionospheres of the Outer Planets and Their Satellites*, *Phys. Chem. Space Ser.*, vol. 15, Springer, New York.

Atreya, S. K., E. Y. Adams, H. B. Niemann, J. E. Demick-Montelara, T. C. Owen, M. Fulchignoni, F. Ferri, and E. H. Wilson (2006), Titan's methane cycle, *Planet. Space Sci.*, *54*, 1177–1187, doi:10.1016/j.pss.2006.05.028.

Bar-Nun, A., and I. Kleinfeld (1989), On the temperature and gas composition in the region of comet formation, *Icarus*, *80*, 243–253, doi:10.1016/0019-1035(89)90136-X.

Bar-Nun, A., G. Notesco, and T. Owen (2007), Trapping of N_2, CO and Ar in amorphous ice application to comets, *Icarus*, *190*, 655–659, doi:10.1016/j.icarus.2007.03.021.

Bar-Nun, A., V. Dimitrov, and M. Tomasko (2008), Titan's aerosols: Comparison between our model and DISR findings, *Planet. Space Sci.*, *56*, 708–714, doi:10.1016/j.pss.2007.11.014.

Bell, J. M., et al. (2010), Simulating the one-dimensional structure of Titan's upper atmosphere: 1. Formulation of the Titan Global Ionosphere-Thermosphere Model and benchmark simulations, *J. Geophys. Res.*, *115*, E12002, doi:10.1029/2010JE003636.

Coates, A. J., F. J. Crary, G. R. Lewis, D. T. Young, J. H. Waite, and E. C. Sittler (2007), Discovery of heavy negative ions in Titan's ionosphere, *Geophys. Res. Lett.*, *34*, L22103, doi:10.1029/2007GL030978.

Crary, F. J., H. T. Smith, D. Reisenfeld, and D. T. Young (2009), Upper limits on the abundance of carbon-bearing ions near the orbit of Titan, paper presented atInternational Conference on Magnetospheres of the Outer Planets, Europlanet, Cologne, Germany.

Crary, F. J., H. T. Smith, D. Reisenfeld, and D. T. Young (2010), Upper limits on carbon group ions near the orbit of Titan: Implications ror methane escape from Titan, paper presented at 38th Assembly of the Committee on Space Research, Bremen, Germany.

Cui, J., R. V. Yelle, and K. Volk (2008), Distribution and escape of molecular hydrogen in Titan's thermosphere and exosphere, *J. Geophys. Res.*, *113*, E10004, doi:10.1029/2007JE003032.

Cui, J., et al. (2009), Analysis of Titan's neutral upper atmosphere from Cassini Ion Neutral Mass Spectrometer measurements, *Icarus*, *200*, 581–615, doi:10.1016/j.icarus.2008.12.005.

De La Haye, V., J. H. Waite, T. E. Cravens, A. F. Nagy, R. E. Johnson, S. Lebonnois, and I. P. Robertson (2007a), Titan's corona: The contribution of exothermic chemistry, *Icarus*, *191*, 236–250, doi:10.1016/j.icarus.2007.04.031.

De La Haye, V., et al. (2007b), Cassini Ion and Neutral Mass Spectrometer data in Titan's upper atmosphere and exosphere: Observation of a suprathermal corona, *J. Geophys. Res.*, *112*, A07309, doi:10.1029/2006JA012222.

De La Haye, V., J. H. Waite, T. E. Cravens, S. W. Bougher, I. P. Robertson, and J. M. Bell (2008a), Heating Titan's upper atmosphere, *J. Geophys. Res.*, *113*, A11314, doi:10.1029/2008JA013078.

De La Haye, V., J. H. Waite, T. E. Cravens, I. P. Robertson, and S. Lebonnois (2008b), Coupled ion and neutral rotating model of Titan's upper atmosphere, *Icarus*, *197*, 110–136, doi:10.1016/j.icarus.2008.03.022.

Dimitrov, V., and A. Bar-Nun (1999), A model of energy-dependent agglomeration of hydrocarbon aerosol particles and implication to Titan's aerosols, *J. Aerosol Sci.*, *30*, 35–49.

Dimitrov, V., and A. Bar-Nun (2002), Aging of Titan's aerosols, *Icarus*, *156*, 530–538, doi:10.1006/icar.2001.6802.

Dimitrov, V., and A. Bar-Nun (2003), Hardening of Titan's aerosols by their charging, *Icarus*, *166*, 440–443, doi:10.1016/S0019-1035(03)00234-3.

Flasar, F. M., et al. (2005), Titan's atmospheric temperatures, winds, and composition, *Science*, *308*, 975–978, doi:10.1126/science.1111150.

Fulchignoni, M., et al. (2005), In situ measurements of the physical characteristics of Titan's environment, *Nature*, *438*, 785–791, doi:10.1038/nature04314.

Hansen, C. J., L. Esposito, A. I. F. Stewart, J. Colwell, A. Hendrix, W. Pryor, D. Shemansky, and R. West (2006), Enceladus' water vapor plume, *Science*, *311*, 1422–1425, doi:10.1126/science.1121254.

Hunten, D. M. (1973), The escape of H_2 from Titan, *J. Atmos. Sci.*, *30*, 726–732.

Jacovi, R., and A. Bar-Nun (2008), Removal of Titan's noble gases by their trapping in its haze, *Icarus*, *196*, 302–304, doi:10.1016/j.icarus.2008.02.014.

Johnson, R. E., O. J. Tucker, M. Michael, E. C. Sittler, D. T. Young, and J. H. Waite (2009), Mass loss processes in Titan's upper atmosphere, in *Titan From Cassini-Huygens*, edited by R. Brown, chap. 15, 373–392, Springer, New York.

Krasnopolsky, V. A. (2009), A photochemical model of Titan's atmosphere and ionosphere, *Icarus*, *201*, 226–256, doi:10.1016/j.icarus.2008.12.038.

Lavvas, P. P., A. Coustenis, and I. M. Vardavas (2008a), Coupling photochemistry with haze formation in Titan's atmosphere, part I: Model description, *Planet. Space Sci.*, *56*, 27–66, doi:10.1016/j.pss.2007.05.026.

Lavvas, P. P., A. Coustenis, and I. M. Vardavas (2008b), Coupling photochemistry with haze formation in Titan's atmosphere, part II: Results and validation with Cassini/Huygens data, *Planet. Space Sci.*, *56*, 67–99, doi:10.1016/j.pss.2007.05.027.

Lebonnois, S. E., E. L. O. Bakes, and C. P. McKay (2003), Atomic and molecular hydrogen budget in Titan's atmosphere, *Icarus*, *161*, 474–485, doi:10.1016/S0019-1035(02)00039-8.

Lee, A. Y., and G. Hanover (2005), Cassini spacecraft attitude control flight performance, in *Proceedings of the AIAA Guidance, Navigation, and Control Conference*, pp. 8–74, Am. Inst. of Aeronaut. and Astronaut., New York.

Liang, M.-C., Y. L. Yung, and D. E. Shemansky (2007), Photolytically generated aerosols in the mesosphere and thermosphere of Titan, *Astrophys. J.*, *661*, L199–L202, doi:10.1086/518785.

Lorenz, R. D., et al. (2008), Titan's inventory of organic surface materials, *Geophys. Res. Lett.*, *35*, L02206, doi:10.1029/2007GL032118.

Magee, B. A., J. H. Waite, K. E. Mandt, J. Westlake, J. Bell, and D. A. Gell (2009), INMS-derived composition of Titan's upper atmosphere: Analysis methods and model comparison, *Planet. Space Sci.*, *57*, 1895–1916, doi:10.1016/j.pss.2009.06.016.

Mandt, K. E., J. H. Waite, W. Lewis, B. Magee, J. Bell, J. Lunine, O. Mousis, and D. Cordier (2009), Isotopic evolution of the major constituents of Titan's atmosphere based on Cassini data, *Planet. Space Sci.*, *57*, 1917–1930, doi:10.1016/j.pss.2009.06.005.

Müller-Wodarg, I. C. F., R. V. Yelle, J. Cui, and J. H. Waite (2008), Horizontal structures and dynamics of Titan's thermosphere, *J. Geophys. Res.*, *113*, E10005, doi:10.1029/2007JE003033.

Niemann, H. B., et al. (2005), The abundances of constituents of Titan's atmosphere from the GCMS instrument on the Huygens probe, *Nature*, *438*, 779–784.

Notesco, G., and A. Bar-Nun (1997), Trapping of methanol, hydrogen cyanide, and n-hexane in water ice, above its transformation temperature to the crystalline form, *Icarus*, *126*, 336–341, doi:10.1006/icar.1996.5654.

Porco, C. C., et al. (2006), Cassini observes the active south pole of Enceladus, *Science*, *311*, 1393–1401, doi:10.1126/science.1123013.

Ridley, A. J., Y. Deng, and G. Tóth (2006), The global ionosphere thermosphere model, *J. Atmos. Terr. Phys.*, *68*, 839–864, doi:10.1016/j.jastp.2006.01.008.

Sarani, S., and A. Y. Lee (2009), Reconstruction of Titan atmospheric density using Cassini guidance, navigation, and control data, in *Proceedings of the AIAA Guidance, Navigation, and Control Conference*, Abstr. 5763, Am. Inst. of Aeronaut. and Astronaut., New York.

Sekine, Y., H. Imanaka, T. Matsui, B. N. Khare, E. L. O. Bakes, C. P. McKay, and S. Sugita (2008a), The role of organic haze in Titan's atmospheric chemistry. I. Laboratory investigation on heterogeneous reaction of atomic hydrogen with Titan tholin, *Icarus*, *194*, 186–200, doi:10.1016/j.icarus.2007.08.031.

Sekine, Y., S. Lebonnois, H. Imanaka, T. Matsui, E. L. O. Bakes, C. P. McKay, B. N. Khare, and S. Sugita (2008b), The role of organic haze in Titan's atmospheric chemistry. II. Effect of heterogeneous reaction to the hydrogen budget and chemical composition of the atmosphere, *Icarus*, *194*, 201–211, doi:10.1016/j.icarus.2007.08.030.

Shemansky, D. E., A. I. F. Stewart, R. A. West, L. W. Esposito, J. T. Hallett, and X. Liu (2005), The Cassini UVIS stellar probe of the Titan atmosphere, *Science*, *308*, 978–982, doi:10.1126/science.1111790.

Sittler, E. C., R. E. Hartle, J. F. Cooper, R. E. Johnson, H. T. Smith, M. D. Shappirio, and D. J. Simpson (2008), Methane group ions in Saturn's outer magnetosphere, in *Bull. Am. Astron. Soc.*, *40*, 448.

Smith, H. T., R. E. Johnson, M. E. Perry, A. M. Rymer, and T. A. Cassidy (2009), The influence of neutrals on Saturn's magnetosphere, paper presented at International Conference on Magnetospheres of the Outer Planets, Europlanet, Cologne, Germany.

Strobel, D. F. (2008), Titan's hydrodynamically escaping atmosphere, *Icarus*, *193*, 588–594, doi:10.1016/j.icarus.2007.08.014.

Strobel, D. F. (2009), Titan's hydrodynamically escaping atmosphere: Escape rates and the structure of the exobase region, *Icarus*, *202*, 632–641, doi:10.1016/j.icarus.2009.03.007.

Tian, F., J. F. Kasting, H. Liu, and R. G. Roble (2008), Hydrodynamic planetary thermosphere model: 1. Response of the Earth's thermosphere to extreme solar EUV conditions and the significance of adiabatic cooling, *J. Geophys. Res.*, *113*, E05008, doi:10.1029/2007JE002946.

Tucker, O. J., and R. E. Johnson (2009), Thermally driven atmospheric escape: Monte Carlo simulations for Titan's atmosphere, *Planet. Space Sci.*, *57*, 1889–1894, doi:10.1016/j.pss.2009.06.003.

Vuitton, V., R. V. Yelle, and V. G. Anicich (2006), The nitrogen chemistry of Titan's upper atmosphere revealed, *Astrophys. J.*, *647*, L175–L178, doi:10.1086/507467.

Waite, J. H., D. T. Young, T. E. Cravens, A. J. Coates, F. J. Crary, B. Magee, and J. Westlake (2007), The process of tholin formation in Titan's upper atmosphere, *Science*, *316*, 870–875, doi:10.1126/science.1139727.

Wilson, E. H., and S. K. Atreya (2004), Current state of modeling the photochemistry of Titan's mutually dependent atmosphere and ionosphere, *J. Geophys. Res.*, *109*, E06002, doi:10.1029/2003JE002181.

Yelle, R. V., N. Borggren, V. de La Haye, W. T. Kasprzak, H. B. Niemann, I. Müller-Wodarg, and J. H. Waite (2006), The vertical structure of Titan's upper atmosphere from Cassini Ion Neutral Mass Spectrometer measurements, *Icarus*, *182*, 567–576, doi:10.1016/j.icarus.2005.10.029.

Yelle, R. V., J. Cui, and I. C. F. Müller-Wodarg (2008), Methane escape from Titan's atmosphere, *J. Geophys. Res.*, *113*, E10003, doi:10.1029/2007JE003031.

A. Bar-Nun, Department of Geophysics and Planetary Sciences, Tel Aviv University, Tel Aviv 69978, Israel.

J. M. Bell, A. D. DeJong, V. De La Haye, G. Fletcher, D. Gell, B. A. Magee, and J. H. Waite Jr., Division of Space Science and Engineering, Southwest Research Institute, 6220 Culebra Rd., PO Box 28510, San Antonio, TX 78228, USA.

S. W. Bougher, A. J. Ridley, and G. Toth, Department of Atmospheric, Oceanic, and Space Sciences, University of Michigan, Ann Arbor, MI 48109, USA.

R. Jacovi, Ice Spectroscopy Laboratory, Jet Propulsion Laboratory, California Institute of Technology, 4800 Oak Grove Dr., Pasadena, CA 91109, USA.

K. E. Mandt and J. Westlake, Department of Physics and Astronomy, University of Texas at San Antonio, San Antonio, TX 78249, USA.